Design, Implementation, and Testing of an Adaptive Optics Test-Bench

by

Brian Peter Wallace
B.Sc., University of Victoria, 1999

A Thesis Submitted in Partial Fulfillment of the
Requirements for the Degree of

INTERDISCIPLINARY MASTER OF APPLIED SCIENCE

in the Department of Mechanical Engineering

Abstract

The purpose of this research project was to design and implement an adaptive optics testbench and to evaluate the effectiveness of the components and completed system. The optical design requirements are discussed and a design presented that incorporates a turbulence generator, tip-tilt mirror, 140 actuator MEMS deformable mirror, Shack-Hartmann wavefront sensor, and a science camera. Key operating characteristics of the opto-mechanical components are investigated including actuator stroke and linearity, influence function, frequency response, and noise. Two controllers are described for zonal and modal operation of the adaptive optics system and are successfully demonstrated in closed loop operation. System performance is investigated from image quality and frequency response perspectives. Recommendations for future developments to both hardware and the control system are made.

Supervisor: Dr. C. Bradley, (Department of Mechanical Engineering)

Table of Contents

Abstract ii

Table of Contents iii

List of Tables v

List of Figures vi

Acknowledgments viii

Dedication ix

1 Introduction 1

1.1 Atmospheric Turbulence 1

1.2 Adaptive Optics 3

2 Optical Design 6

2.1 Optical Conjugation 6

2.2 Tip-Tilt Mirror Test Design 8

2.3 Adaptive Optics Test Bench 9

2.3.1 Turbulence Generator 12

3 Wavefront Sensors 20

3.1 Wavefront Sensor Review 20

3.1.1 Curvature Sensor 20

3.1.2 Shack-Hartmann Sensor 21

3.2 Test-Bed Wavefront Sensor Design 23

3.2.1 Camera 23

3.2.2 Lenslet Array 24

3.2.3 Opto-Mechanical Design 27

3.2.4 Computer Interface and Software 28

4 Deformable Mirrors **30**
4.1 Deformable Mirror Review 30
4.1.1 Segmented Mirror 30
4.1.2 Continuous Mirrors 31
4.2 MEMS Deformable Mirror 34
4.2.1 Bending Theory 36

5 Control System **38**
5.1 Reconstructor 40
5.1.1 Zonal Reconstructor 41
5.1.2 Modal Reconstructor 42

6 Results **45**
6.1 Tip-Tilt Mirror Characterization 45
6.1.1 Angular Range and Linearity 45
6.1.2 Frequency Response 46
6.2 DM Characterization 46
6.2.1 Stroke and Linearity 48
6.2.2 Response Time 50
6.2.3 Influence Function 50
6.2.4 Zernike Mode Representation 52
6.3 Wavefront Sensor Characterization 55
6.3.1 Noise 55
6.3.2 Frame Rate 61
6.4 Image Quality 61
6.4.1 Zonal Controller 63
6.4.2 Modal Controller 65
6.5 Frequency Response 69

7 Conclusion **72**
7.1 Optical Design 72
7.2 AO System Components 72
7.3 System Performance 73
7.4 Future Work 74

Bibliography **79**

A Optical Design **80**
A.1 Turbulence Generator Foreoptics 80
A.2 Wavefront Sensor Path 82
A.3 Science Path 85

List of Tables

2.1 Raytrace data showing the projection of DM position on the lenslet array. . 11
2.2 Turbulence generator atmospheric properties for given ΔT 14
2.3 Angular resolution raytrace data 17

3.1 Lenslet array properties 27

4.1 BM DM mechanical properties. 36

5.1 Orthogonal modal basis functions defined on a rectangular grid 42

List of Figures

1.1 A representative Adaptive Optics system for a telescope. 4

2.1 Object and image conjugate planes for a 50mm focal length achromatic lens. 7
2.2 Two lens conjugate system that preserves collimation. 7
2.3 Tip-Tilt mirror test layout. 8
2.4 Adaptive optics test-bed optical design incorporating a tip-tilt mirror, deformable mirror, wavefront sensor and science camera. 10
2.5 Schematic of actuator registration in the lenslet plane 12
2.6 Turbulence generator mechanical design. 13
2.7 Turbulence power spectrum showing Kolmogorov power laws 15
2.8 Turbulence generator optics. 16
2.9 Adaptive Optics testbed optical design including both science and wfs paths 18
2.10 Photograph of the adaptive optics testbed. 19

3.1 Operation of a curvature sensor 21
3.2 Operation of a Shack-Hartmann wavefront sensor 22
3.3 Quad-cell detector for centroid measurement 23
3.4 Exploded view of Shack-Hartmann wavefront sensor. 28
3.5 Wavefront sensor data flow chart. 29

4.1 Segmented mirror types. 31
4.2 Monolithic piezoelectric mirror 32
4.3 Bimorph mirror schematic and typical electrode pattern. 33
4.4 Membrane mirror schematic. 33
4.5 Boston Micromachines DM schematic 35

5.1 Control system of the adaptive optics test-bed 39
5.2 DM actuator map 44

6.1 Tip-tilt mirror angular displacement of each axis. 46
6.2 Schematic of fiber interferometer setup with DM. 47
6.3 Circuit diagram of a single channel of the DM driver diagnostic box. 48

6.4 DM displacement for an increasing and decreasing voltage cycle. 49
6.5 DM displacement response time to a voltage step 50
6.6 Deformable mirror single actuator influence function at 75%. 51
6.7 0° and 45° cross-sections of DM influence function. 52
6.8 Individual, superimposed, and 2-actuator influence function cross-sections. . 53
6.9 RMS displacement of the Zernike mode, DM best fit, and residual error. . . 54
6.10 RMS displacement of the Zernike mode, DM best fit, and residual error for a 1024 actuator DM. 55
6.11 DM surface fit to Z_2^2 56
6.12 DM surface fit to Z_6^6 57
6.13 Flat field image cross-section with overscan region. 58
6.14 Average bias frame 59
6.15 Flat field image. 59
6.16 Open loop centroid variation without turbulence. 60
6.17 Theoretical diffraction limited and turbulence limited point spread functions. 62
6.18 Singular values of the zonal reconstructor 63
6.19 Strehl ratio and FWHM for the zonal controller as a function of SVD cutoff. 64
6.20 Tilt actuator content for each eigenmode of the Zonal SVD. 65
6.21 Strehl improvement ratio and FWHM as a function of zonal controller gain 66
6.22 Singular values of the modal reconstructor 67
6.23 Strehl improvement ratio and FWHM for the modal controller as a function of SVD cutoff. 67
6.24 Tilt actuator magnitude in modal eigenmodes. 68
6.25 Strehl ratio and FWHM as a function of modal controller gain 69
6.26 Encircled energy for modal and zonal controllers. 70
6.27 Rejection ratios for the zonal and modal controllers 71

Acknowledgements

There are a number of people I'd like to thank for their support and contributions towards this project. I'd like to thank my supervisor Dr. Colin Bradley for funding the project and guiding it towards success, and Dr. Harvey Richardson for introducing me to optical design and answering all my questions. I'd also like to thank Dr. Rodolphe Conan for his valuable insight and input towards the project.

The broad scope of the AO test-bench required the contributions of several other researchers for success. I'd like to thank Onur Keskin for his work on the turbulence generator, Jeff Kennedy for mechanical design and machining, Peter Hampton for control system development, and Aaron Hilton for software development.

Finally, I'd like to thank my friends and family for their support and encouragement through everything.

For my wife, Julia.

Chapter 1

Introduction

1.1 Atmospheric Turbulence

In the absence of atmosphere, the best possible image of a stellar point source by a telescope will be a diffraction limited image. The diffraction limited angular resolution in radians of a circular telescope aperture is given by the well known Fraunhofer diffraction equation

$$\theta = 1.22\frac{\lambda}{d} \tag{1.1}$$

where d is the diameter of the aperture and λ the wavelength of light. In the case of a modern 8 m telescope, the diffraction limited image would have an angular resolution of 8.4×10^{-8} rad $= 0.017''$ (with $\lambda = 550$ nm).

In practice, however, this is rarely achieved. The resolution is limited by blurring, fracturing, and random displacements of the image caused by the atmosphere. The limiting angular resolution is typically referred to as "seeing" in the astronomy community. Rarely is the seeing better than $0.5''$ at even the best observatory locations in the world [6, 9, 43].

This blurring is caused by random inhomogeneities that exist in the temperature distribution of the atmosphere. These variations originate primarily with the diurnal heating and cooling of the earth during its rotation. These large scale variations are broken down into turbulent eddies with smaller spatial scales by wind. Since the index of refraction of air varies with temperature (an empirical relation can be found in [30]), these eddies vary

the optical path length of rays passing through them, hence varying the phase across a wavefront. A quantity commonly used to describe the variance of the refractive index is the index structure coefficient, C_N^2, defined by:

$$C_N^2 = \rho^{-2/3} \left\langle |n(\boldsymbol{r}) - n(\boldsymbol{r} + \boldsymbol{\rho})|^2 \right\rangle . \tag{1.2}$$

The integral of C_N^2 along the line of sight gives a measure of the seeing. Since the atmosphere is usually considered to be stratified parallel layers, the index structure function depends only on the height above ground.

When plane waves from a stellar source strike the atmosphere, they are distorted, resulting in a corrugated wavefront. When focussed by a telescope, the distorted wavefront forms a blurred image. A rigorous treatment of wave propagation through the atmosphere can be found in the literature [38, 41].

Fried's parameter, r_0, provides a link between the scale of the turbulent eddies and the achievable resolution. Originally described as the diameter of an optical heterodyne receiver beyond which turbulence significantly limits performance [12], it was later derived that the resolution achieved over a long exposure would be that obtained with a diffraction limited lens of diameter r_0 in the absence of atmosphere [13], i.e.:

$$\theta = 1.22 \frac{\lambda}{r_0} \tag{1.3}$$

The implication of this result is that regardless of the diameter of an Earth-based telescope, its resolution will be limited to that of a telescope of diameter r_0. Based on experimental data, an expression for the median value of r_0 was derived [14]:

$$(r_0)_{\text{median}} = 0.114 \left(\lambda/5.5 \times 10^{-7}\right)^{3/5} (\sec \gamma)^{-3/5} \tag{1.4}$$

where r_0 is measured in meters and γ is the zenith angle of the observations. It is worth noting that in actuality these values will be dependant on geographic location, weather, etc. but provide a reasonable estimate for this discussion. This basic relationship shows that the effect of turbulence is reduced at longer wavelengths and when observing through

less atmosphere (i.e. more directly overhead). For $\lambda = 550$ nm, r_0 has a median value of 11.4 cm overhead, an effective aperture 70 times smaller than an 8 m telescope. Reducing, or even eliminating, this resolution limitation provides the motivation for adaptive optics.

1.2 Adaptive Optics

While light collecting power alone is a significant advantage to increasing the size of ground based telescopes, without the added benefit of increased resolution, it cannot justify the dramatically increased cost of these structures. A system for real-time correction of atmospheric effects is desirable for achieving high resolution images over long exposures with large telescopes. We refer to such a system as "Adaptive Optics".

To compensate for turbulence induced distortions, a means of detecting the phase errors present in the wavefront is required. Such a device is referred to as the wavefront sensor. A control system interprets the wavefront sensor data and converts it to actuator error signals for the corrective element(s). A representative astronomical adaptive optics system is shown in Figure 1.1. Starlight, effectively a plane wavefront due to distance, reaches Earth and is distorted by the atmosphere. The light is collected by the telescope and a collimating mirror images the telescope aperture on the corrective element, in this case a deformable mirror. Following this, a beamsplitter divides the light, sending some to the wavefront sensor for analysis, the rest is re-imaged on the science camera. A control system completes the feedback loop between wavefront sensor and corrector.

A first order correction involves the removal of the random displacements of the image. This is typically referred to as tip-tilt correction or fast guiding. Noll showed that perfect correction of tip and tilt would yield the single largest improvement in image quality [32], an 87% reduction in the phase variance. Tyler also demonstrated that the bandwidth required for tip-tilt correction is about nine times lower than that required for complete atmospheric compensation [45].

These two advantages were exploited, as well as the relative simplicity of a two degree-of-freedom system, in early compensation devices. Leighton's design for the Mt. Wilson telescope in 1956 translated a lens at up to 2 Hz to achieve the best planetary images

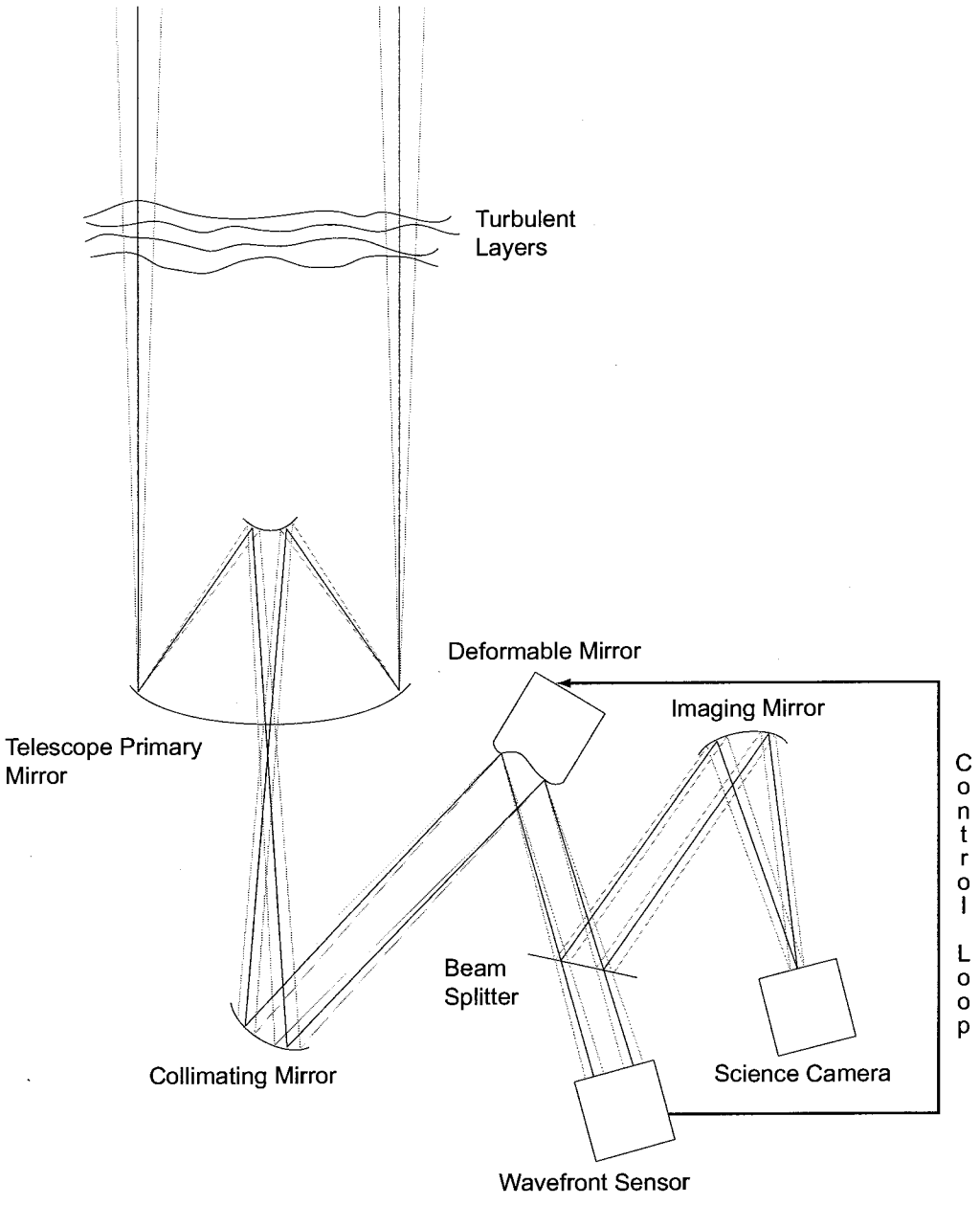

Figure 1.1: A representative Adaptive Optics system for a telescope.

of the era [29]. With materials and electronics advancements, HRCam for the Canada-France-Hawaii Telescope was constructed in 1989 using a piezo-electric steering mirror able to operate at 500 Hz [31].

Higher order correction was first proposed by Horace W. Babcock [2]. As a correcting element, he proposed the use of an Eidophor, a thin film of oil covering a mirror. The oil film is distorted by electrostatic forces when a charge is deposited upon it by traditional CRT methods. As a wavefront sensor, the schlieren pattern created by a rotating knife edge at the telescope focus, recorded by an image orthicon. While never built, this proposal paved the way for modern adaptive optics.

Adaptive optics development proceeded primarily under military programs, but in 1977, Hardy et al. demonstrated a 21-actuator monolithic piezoelectric mirror operating in closed loop over a 300 m horizontal propagation path [17]. Diffraction-limited astronomical images were not achieved until 1990 with the "COME-ON" system on the 1.52 m telescope at the Observatoire de Haute Provence [39]. This system used a 19-actuator deformable mirror, a separate tip-tilt mirror, and a Shack-Hartmann style wavefront sensor. Adaptive optics has rapidly progressed since then and has been incorporated in nearly every new observatory.

As new concepts in adaptive optics arise it is desirable to model their operation before full-scale construction. While computer simulations may be successful it is frequently more desirable to work with a hardware system. This thesis presents the optical design, component characterization, and closed loop testing of a laboratory based adaptive optics system. The goal of the adaptive optics test-bed is to allow the evaluation of new hardware and control systems for advanced adaptive optics research.

Chapter 2

Optical Design

A series of optical designs were realised during the development process of the adaptive optics test-bed. Before incorporation into the AO test-bed, the mechanical properties of the tip-tilt mirror were determined using a straightforward optical setup. The tip-tilt mirror was then incorporated into a more elaborate design including the deformable mirror and wavefront sensor as well for the first AO system. Ultimately, this design was expanded to include a turbulence generator. The final two AO optical designs make use of optical conjugates for correct operation.

2.1 Optical Conjugation

The definition of conjugate points in an optical system are two points on the principal axis of a mirror or lens positioned such that light emitted from one will be focussed at the other. This is illustrated in Figure 2.1 with a ⊘ 25 mm 50 mm focal length achromatic lens. The scale has been emphasized to more clearly show the rays. In the case of an object point at infinity the input light is collimated and the conjugate point is at the focal length of the lens. This concept is easily understood as a camera system: the camera lens focuses the subject on the film plane, hence the object and film planes are conjugate to each other.

Wavefront sensors and corrective elements are typically made conjugate to the source of turbulence. In this way, the primary source of disturbance is most accurately sampled and corrected. However, both the wavefront sensor and corrective devices require collimated

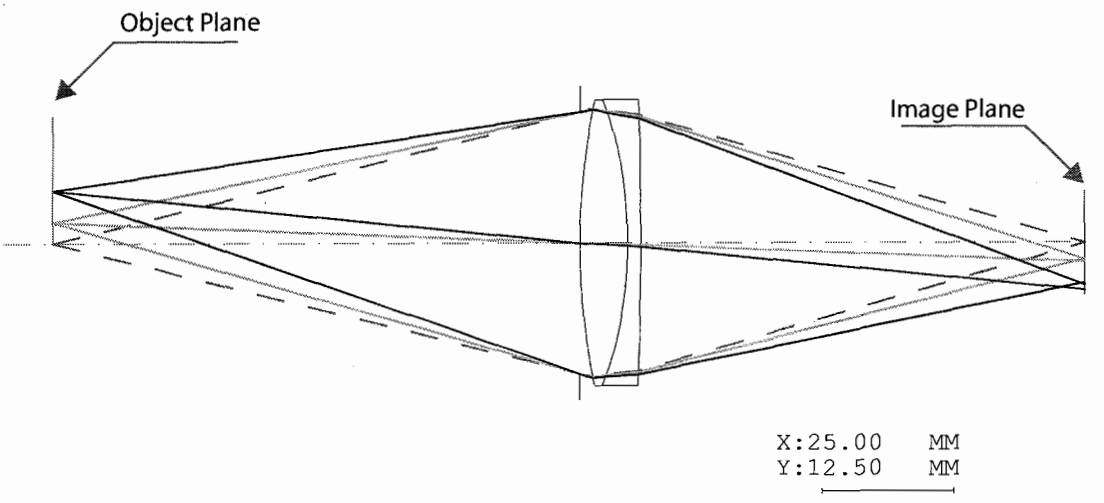

Figure 2.1: Object and image conjugate planes for a 50mm focal length achromatic lens.

light to function correctly. While conjugate points exist with a single lens or imaging system, it is not possible to preserve collimation as well.

By pairing two lenses separated by the sum of their focal lengths, it is possible to reimage an object plane (typically the pupil) while preserving the collimation of the light. This is illustrated in Figure 2.2 with a raytrace of a pair of achromat lenses separated by their focal lengths. Collimated light from three field angles is shown entering the pupil plane, similar to light entering a telescope, and is focused by the first lens. The second lens recollimates the light but also forms a conjugate image of the pupil plane as evidenced by the intersection of the three field angles.

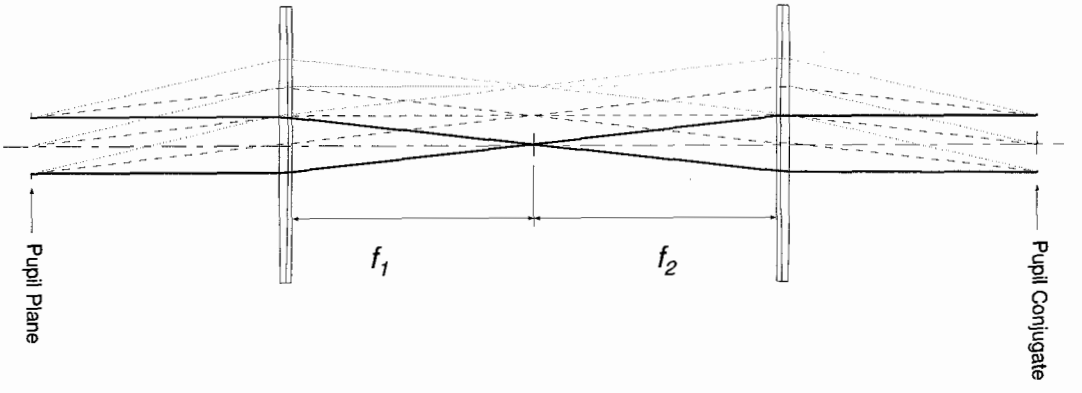

Figure 2.2: Two lens conjugate system that preserves collimation.

With identical lenses, the image of the pupil is inverted but there is no change of magnification. By pairing lenses of different focal lengths, the magnification of the image can be controlled via the simple relation $M = f_2/f_1$.

2.2 Tip-Tilt Mirror Test Design

To evaluate the mechanical properties of the tip-tilt mirror the optical setup in Figure 2.3 was utilised. A fiber coupled laser diode was collimated by a Melles Griot LAO022 lens with 30 mm focal length. The collimated light was incident on a 3 mm $\times$ 1 mm rectangular slit. The long axis of the slit was oriented in the same direction as the tip-tilt mirror axis to be tested. The rectangular beam was reflected at near-normal incidence from the centre of the tip-tilt mirror. A knife edge was placed in the beam just before a 100 mm square photo-diode. With zero volts on the tip-tilt mirror, the knife edge completely blocked the beam.

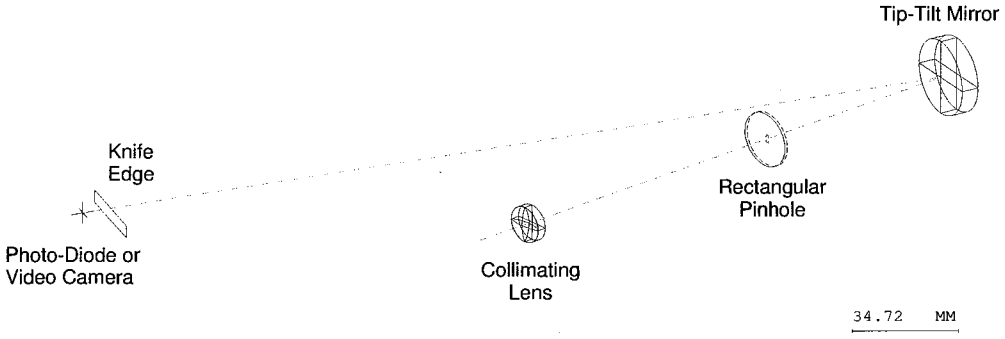

Figure 2.3: Tip-Tilt mirror test layout.

To test bandwidth, the mirror is oscillated at known frequencies with fixed amplitude perpendicular to the knife edge. As the rectangular beam moves across the knife edge, the photo-diode produces a voltage proportional to the amount of light it receives. When the -3 dB frequency of the mirror is reached, the voltage response from the photo-diode will correspondingly be reduced by 3 dB. The second axis of the tip-tilt mirror can be tested by rotating the slit and knife edge 90°.

By removing the rectangular slit and knife edge and replacing the photo-diode by a video camera, the angular range and linearity of the tip-tilt mirror can be measured. The

displacement for a given input voltage is measured by the camera and converted into physical units. The angular displacement of the light ray can be determined using the trigonometric identity $\theta = \arctan(opp/adj)$ since the distance between the mirror and camera is known. Note that this angle must be halved to give the actual angular change of the tip-tilt mirror.

2.3 Adaptive Optics Test Bench

The design requirements for the initial testing of the integrated components of the AO test-bed were as follows:

1. Generate a light source to fill the deformable mirror (3.3×3.3 mm).
2. Establish conjugation between pupil, tip-tilt mirror, deformable mirror, and wavefront sensor.
3. Light incident on the tip-tilt and deformable mirrors and wavefront sensor must be collimated.
4. Provide access to a pupil image plane for a science camera.
5. Demagnify deformable mirror image such that actuators are well registered with the lenslet array of the wavefront sensor (300μm $\rightarrow$ 188μm).
6. Use off-the-shelf optics.

Figure 2.4 illustrates the optical design that met these objectives. The laser light source was a Melles Griot 5 mW HeNe (632.8 nm) laser coupled to a single mode fiber. The diverging light from the fiber was collimated by a Melles Griot LAO022 lens with 30 mm focal length. This produced a collimated beam of 5.2 mm diameter, slightly larger than the 4.67 mm diagonal width of the deformable mirror. The laser output was mounted on a translation stage oriented transverse to the optical axis. This allowed for a tilt to be imposed on the wavefront for testing. The collimating lens is the pupil of the system.

The following lenses are a pair of Edmunds 150 mm focal length achromats. They behave as a relay lens, re-imaging the pupil on the tip-tilt mirror and preserving collimation. These lenses were mounted on an optical rail for positioning.

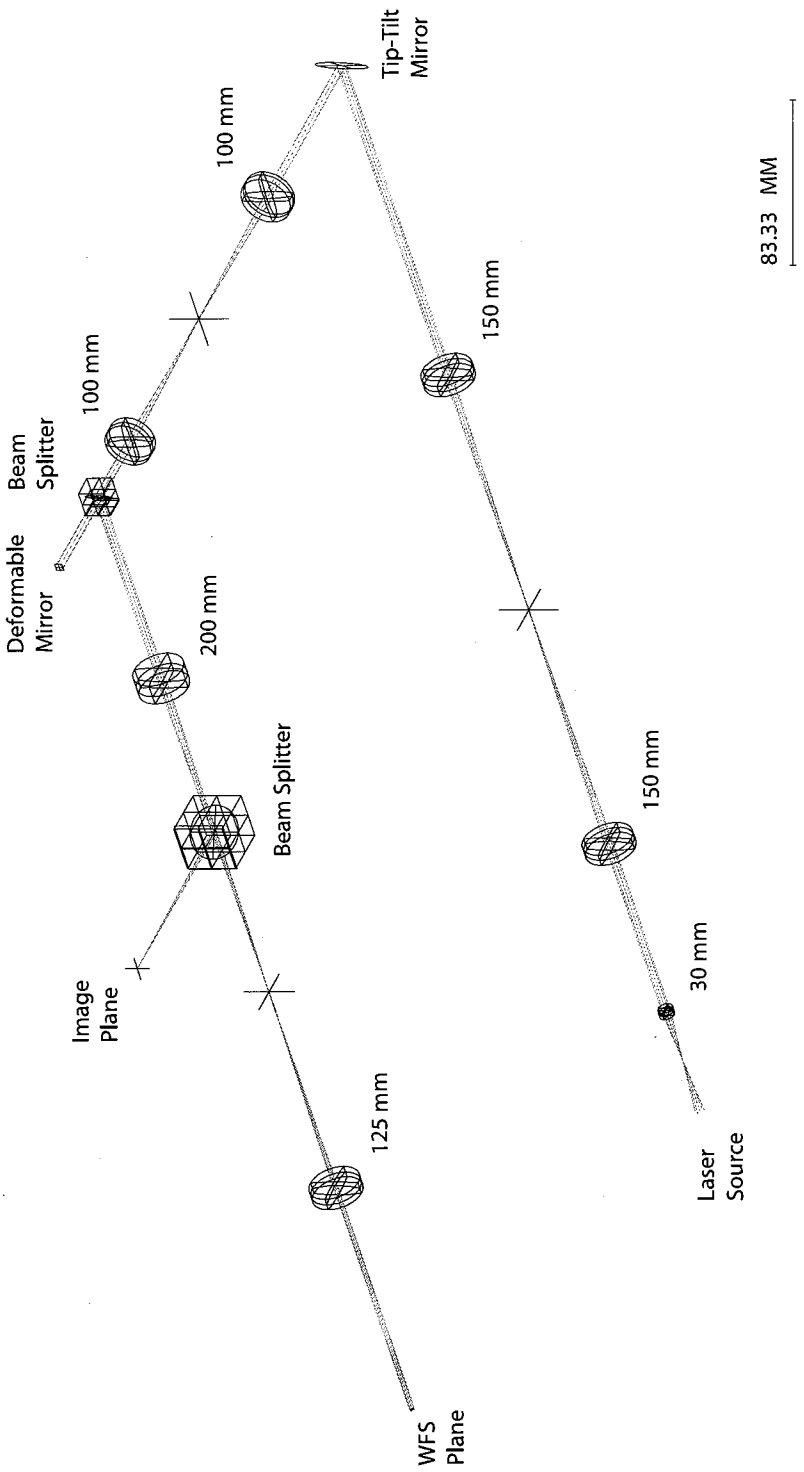

Figure 2.4: Adaptive optics test-bed optical design incorporating a tip-tilt mirror, deformable mirror, wavefront sensor and science camera.

The tip-tilt mirror was clamped to the optics table at a 45° angle. It is followed by another relay lens pair, Edmunds 100 mm focal length achromats. These lenses were mounted on translation stages in line with the optical path for position adjustments.

Following this is a cube beam-splitter (Melles Griot 03 BSC 005). The transmissive path passes to the deformable mirror while the reflective path (not shown) goes to a $\frac{\lambda}{20}$ surface quality reference mirror. This arrangement creates a Michelson type interferometer when both light paths are unobstructed, useful for alignment of the DM. In AO operation, the reference mirror is used for calibration only, that light path is then blocked during closed loop operation.

The third relay lens pair is a 200 mm and 125 mm focal length set of achromats. This pairing gives a magnification factor of 125/200 = 0.625, which should reduce the 300 μm DM actuators to an image of 187.5 μm on the lenslet array. Raytrace data from Table 2.1 shows that a single actuator at the DM centre is well registered with the 188 μm lenslet pitch, and an edge actuator is only misregistered by 4.2 μm. The sign change indicates that the image has been flipped by the lenses.

DM Position (mm)	Position on Lenslet (mm)	Closest Lenslet (mm)
0.3000	-0.1873	-0.1880
1.8000	-1.1238	-1.1280

Table 2.1: Raytrace data showing the projection of DM position on the lenslet array.

Between the two lenses is a 50/50 cube beam-splitter that, on the reflected path, provides access to a focused image for a science camera. The 200 mm lens was mounted on an optical rail along with the beam-splitter. The 125 mm lens was mounted on a translation stage in line with the optical axis for adjustments to ensure collimation.

The wavefront sensor itself was mounted on vertical and horizontal translation stages transverse to the optical axis. This allowed for fine adjustments in position to properly register the image of the DM actuators with the lenslet array. The actuator to lenslet subaperture registration used (see Figure 2.5) was similar to the Fried geometry with slope measurement points centred between four actuators. With an $n \times n$ square actuator layout, it can be seen that this arrangement provides $2(n-1)^2$ slope measurements for n^2 degrees of freedom. Provided that $n \geq 4$, then there are more slope measurements than actuators.

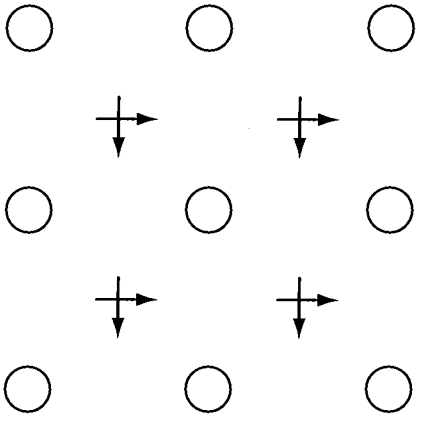

Figure 2.5: Schematic of actuator registration in the lenslet plane. Slope measurements are made at the crosses, actuator centres are at the circles.

2.3.1 Turbulence Generator

For laboratory testing of an AO system, the turbulence generator is a crucial component. It generates the random distortions to the wavefront to test the AO control loop. A number of options were considered including rotating phase plates, fluid mixing box, and a hot air mixing box. Due to its versatility, cost effectiveness, and ease of implementation, a hot air mixing tubulence generator was selected for the AO testbed.

Based on previous work by Jolissaint [22], a hot air turbulence generator was constructed and characterised [25, 26]. Figure 2.6 shows a simplified mechanical design of the turbulence generator. It was constructed from 6 mm thick aluminum plate and has outer dimensions of $57.5 \times 36.5 \times 18.5$ cm. The box is divided into two flow channels 17.3 cm wide with an open mixing zone 17.5 cm long in the centre. The ends of both channels are open to allow air intake and exhaust. Fans and heater coils were mounted at the mouths of the lower channel in the diagram. Following these, a 2 cm thick honeycomb material fills the channel to laminarise the air flow into the mixing zone of the turbulence generator. Two 10 cm diameter windows with low thermal expansion properties were mounted in the sides of the box to allow collimated light to pass through the mixing zone.

The air intake at one end of the channel remains at room temperature (cold intake) while the other intake is heated (hot intake). Both fans were operated at identical fixed velocities. The temperature difference between hot and cold intakes could be varied up to

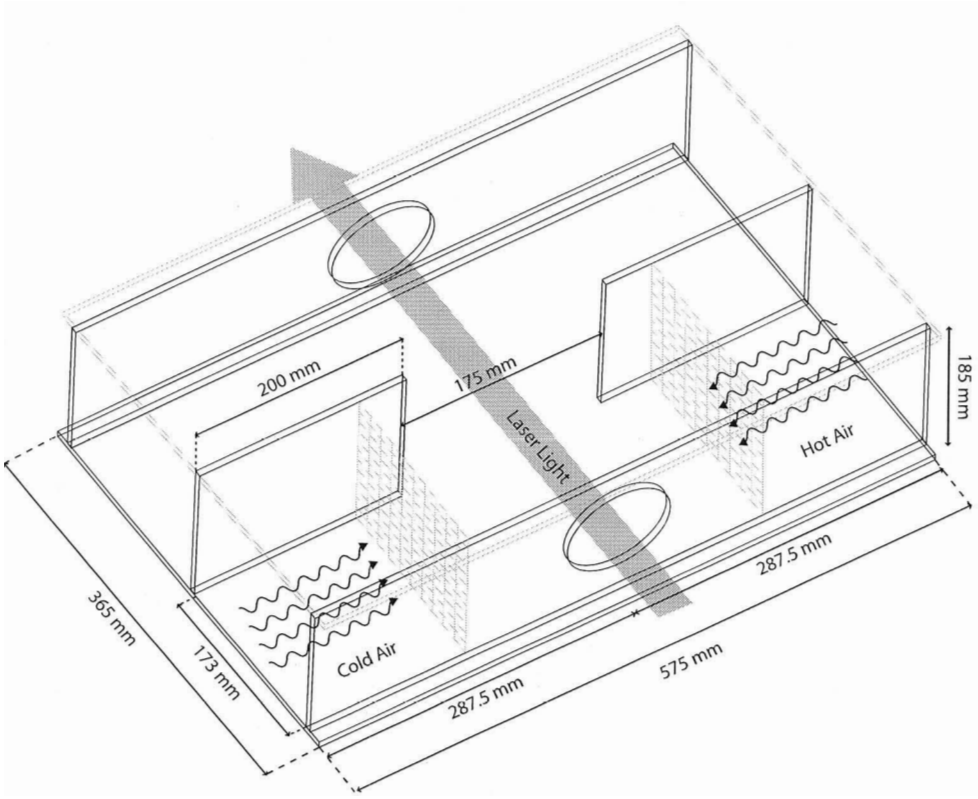

Figure 2.6: Turbulence generator mechanical design.

ΔT $[^\circ K]$	$C_N^2 \Delta h_X$ $[10^{-10} m^{1/3}]$	r_{0_X} $[mm]$	$C_N^2 \Delta h_Y$ $[10^{-10} m^{1/3}]$	r_{0_Y} $[mm]$	$\langle C_N^2 \Delta h \rangle$ $[10^{-10} m^{1/3}]$	$\langle r_0 \rangle$ $[mm]$
33	2.55	2.89	2.21	3.15	2.38	3.01
63	4.28	2.12	3.61	2.35	3.95	2.23
103	4.38	2.09	3.95	2.22	4.17	2.15
133	5.47	1.83	4.83	1.97	5.15	1.90
163	6.16	1.70	5.53	1.82	5.85	1.76

Table 2.2: Turbulence generator atmospheric properties for given ΔT (from Keskin [26]).

$\Delta T = 163°$C assuming room temperature of 21°C. After mixing, the air is able to exhaust though the second channel in the box.

A summary of the atmospheric properties generated is presented in Table 2.2. It can be seen that the turbulator produces isotropic turbulence with r_0 ranging between 1.76 mm and 3.01 mm. The turbulence temporal power spectrum also demonstrates the $-2/3$ and $-11/3$ power laws of Kolmogorov statistics as shown in Figure 2.7. The dashed and solid lines in the figure represent measurements in the x and y directions.

Rather than design an entirely new optical prescription to include the turbulence generator with the other AO components, the design from Section 2.3 was expanded.

The new optical design requirements for the inclusion and operation of the turbulence generator were as follows:

1. Input beam diameter to turbulence generator compatible with desired D/r_0 ratio.
2. Exit beam diameter from new optics of approximately 4.67 mm (to fill DM).
3. Collimated exit beam.
4. Maintain pupil location from previous design in Section 2.3.
5. Ensure science camera angular resolution of at least $1.22\frac{\lambda}{2d}$.

To determine the desired input beam diameter to the turbulence simulator, the number of controlled actuators was considered. Referring to Chapter 5, ten actuators across the diameter of the deformable mirror are controlled. The maximum amount of turbulence we can expect to effectively correct is thus $D/r_0 = 10$. Reviewing the scale of r_0 the turbulence generator can achieve from Table 2.2, at $\Delta T = 103°$K, $D/r_0 = 10$ could be achieved with a beam diamter of 21.5 mm without operating at maximum temperature.

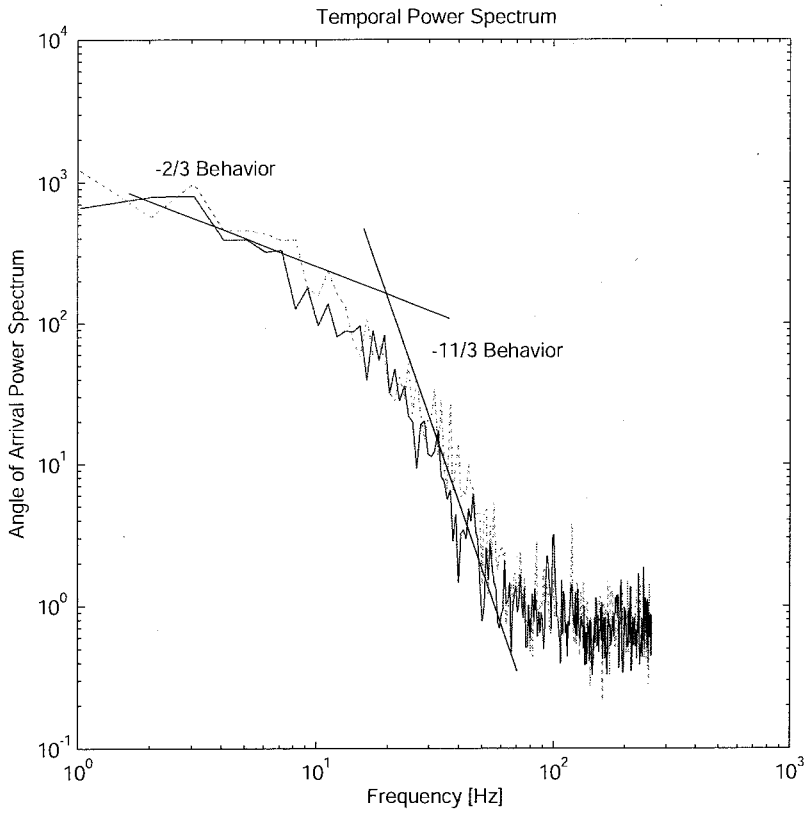

Figure 2.7: Turbulence power spectrum ($\Delta T = 90°C$) showing Kolmogorov power laws (From Jolissaint [23]).

To produce a 21.5 mm beam a new laser with a spatial filter and collimator were used (Melles Griot 09 LSF 011 and 09 LCM 011). A 4 mm focal length microscope objective was paired with a 10 μm pinhole in the spatial filter assembly. This produced a 25 mm diameter beam when used with the collimator. The clear aperture of the following lenses restricts the beam to 22 mm.

After passing through the turbulence generator, demagnifying optics were required to reduce the beam diameter to the desired 4.67 mm. Similarly to the demagnification in Section 2.3, a pair of achromatic lenses with different focal lengths were used. In this case a 200 mm focal length lens was followed by a 60 mm focal length lens, separated by the sum of their focal lengths to preserve collimation. This gave a demagnification factor of $60/200 = 0.3$ which reduced the beam diameter to 6.6 mm (Note that the clear aperture of

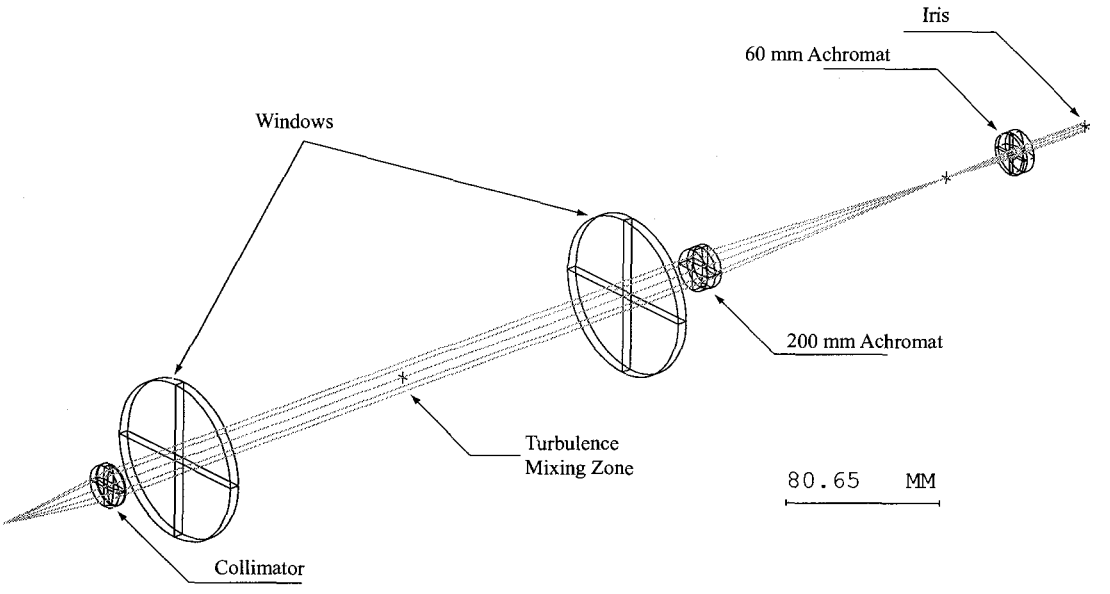

Figure 2.8: Turbulence generator optics.

the lenses was only 22 mm). This diameter slightly larger than the DM aperture is desirable as explained below.

The demagnifying lens pair was followed by an iris diaphragm whose clear aperture was set to approximately 2.74 mm. The iris was located at the same position as the collimation lens of the previous design in Figure 2.4. Since tip and tilt of the beam will originate in the mixing zone of the turbulence simulator, the beam will wander about the optical axis on the iris. By having the iris diameter smaller than the beam diameter, it ensures the iris clear aperture will always be fully illuminated. To the wavefront sensor, this also has the effect of making the turbulence appear to originate at the iris. This property and the limiting aperture defines the iris as the pupil of the system in the same way the collimating lens of the previous design was. The pupil projection on the deformable mirror illuminates ten actuators across the diameter.

A perspective view of the additional optics for the turbulence generator are shown in Figure 2.8. The new collimator is represented by a single lens, though it is a multi-lens system with focusing ability in reality. By removing the laser source and collimator of Figure 2.4 and replacing them with the optics of Figure 2.8, the light source design objectives were met.

A desired quantity derived from the science image is the optical transfer function (OTF). The OTF can be described as the autocorrelation of the pupil, having a diameter d. The OTF can be calculated from the science image via the 2-D inverse Fourier transform. Based on the Nyquist sampling theorem, to compute the OTF without aliasing at the science camera, the image sampling frequency must be at least 1/2D. Equation 1.1 defines the angular resolution of the optical system in the absence of turbulence, where λ is the laser wavelength (632.8 nm) and d is the iris diameter (2.74 mm), thus the science camera pixels should have an angular resolution of at least $\frac{1.22\lambda}{2d}$.

Additionally, the image size with turbulence should not exceed the science camera detector area. From Equation 1.3, knowing the smallest r_0 we plan to operate with (2.15 mm for $D/r_0 = 10$ in the turbulence generator), and accounting for the demagnification in the foreoptics, an image with angular size $\frac{1.22\lambda}{r_0(60/200)}$ should be fully sampled on the CCD.

Table 2.3 shows raytrace data for these two criteria, as well as the approximate angular resolution of a single pixel on the science camera (16 μm). From this data we can see that the angular frequency is well sampled in the diffraction limited case and we are just able to image the aberrated PSF (CCD half-width is 1.05 mm).

	Field Angle (deg)	CCD Position (mm)
$\approx 1.22\lambda/14d$	0.00114	-0.016
$1.22\lambda/2d$	0.00807	-0.11320
$1.22\lambda/r_0(60/200)$	0.06858	-0.96179

Table 2.3: Angular resolution raytrace data

The complete optical layout is illustrated in Figure 2.9 and the optical design can be found in Appendix A. A photo of the completed test-bench is shown in Figure 2.10. This picture was taken from over top of the turbulence generator and shows all of the components that follow it except the iris which has been removed. Note that the optical design was flipped to improve cable routing for the physical implementation.

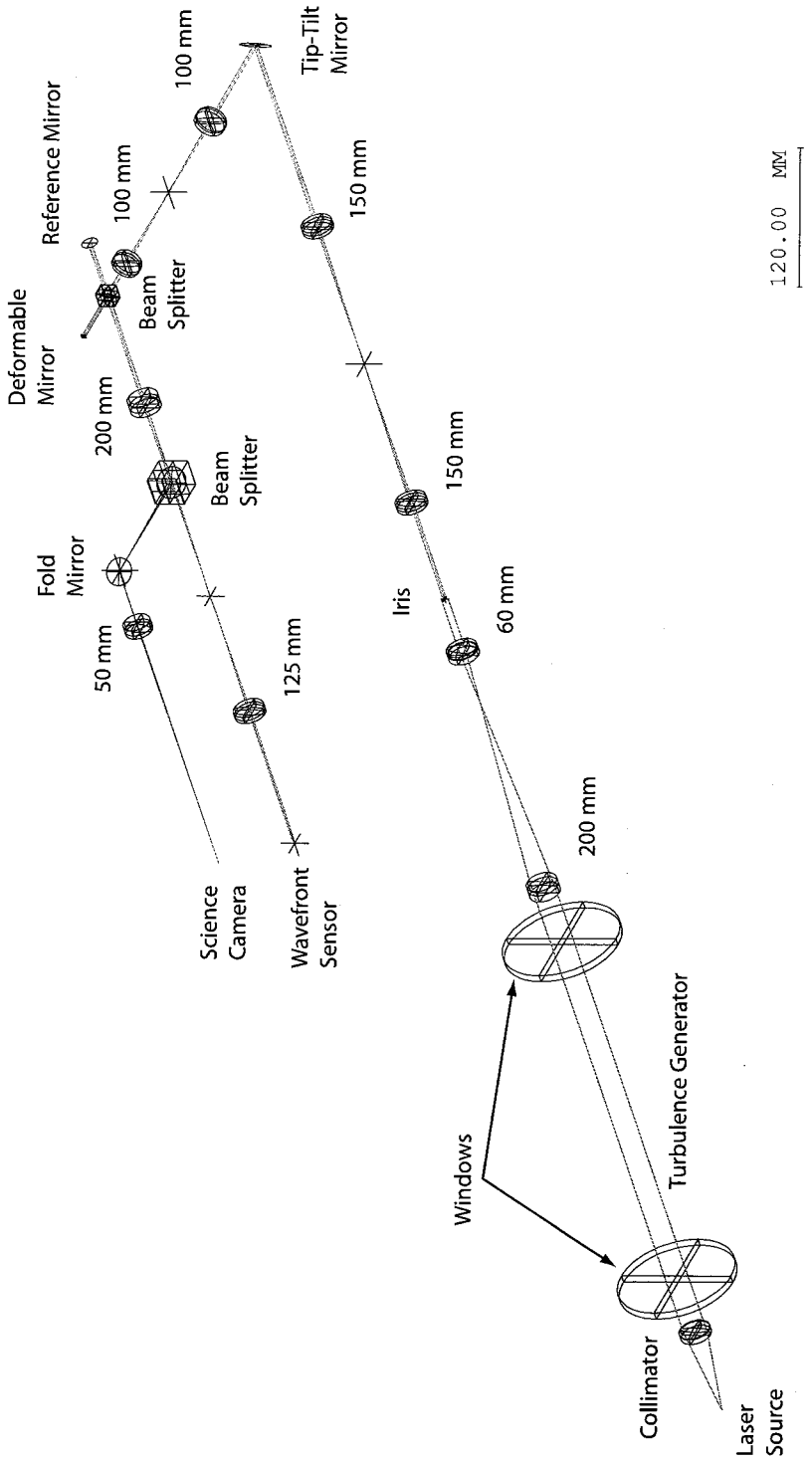

Figure 2.9: Adaptive Optics testbed optical design including both science and wfs paths. Lens focal lengths are indicated.

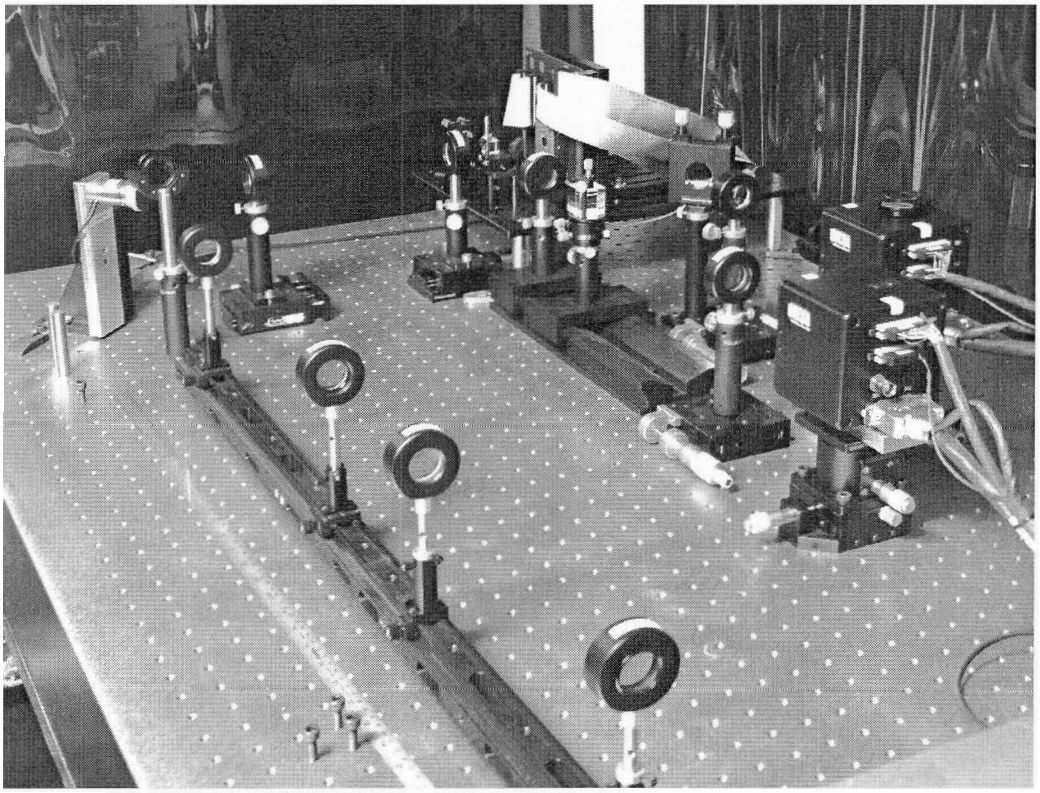

Figure 2.10: Photograph of the adaptive optics testbed.

Chapter 3

Wavefront Sensors

3.1 Wavefront Sensor Review

The wavefront sensor is used to determine the phase delays present in the wavefront. This can be accomplished by measuring the phase directly, measuring the gradient of the phase, or measuring the Laplacian of the phase. Direct phase sensing devices include the Mach-Zehnder interferometer [28], lateral shearing interferometer [17, 48], and phase diversity sensor [21, 34]. The Shack-Hartmann and Pyramid sensors [36] each sample the wavefront slope, while the curvature sensor measures the phase Laplacian. The two most common wavefront sensors in application are the curvature sensor and Shack-Hartmann sensor.

3.1.1 Curvature Sensor

A unique approach to wavefront sensing, measuring wavefront curvature, was proposed by Roddier[37]. The curvature sensor functions as illustrated in Figure 3.1. The illumination distribution, I_1 and I_2, is measured in planes P_1 and P_2 respectively. The plane P_1 lies a distance d before the focus of the lens L, while P_2 is at a distance d beyond the focus. The relationship between illumination and curvature is given by

$$\frac{I_2(\boldsymbol{r}) - I_1(\boldsymbol{r})}{I_2(\boldsymbol{r}) + I_1(\boldsymbol{r})} = \frac{f(f-d)}{2d}\left[\frac{\partial}{\partial \boldsymbol{n}} z(f\boldsymbol{r}/d)\delta_c + \nabla^2 z(f\boldsymbol{r}/d)\right] \tag{3.1}$$

where δ_c is a linear impulse distribution around the pupil edge, weighted by the radial tilt,

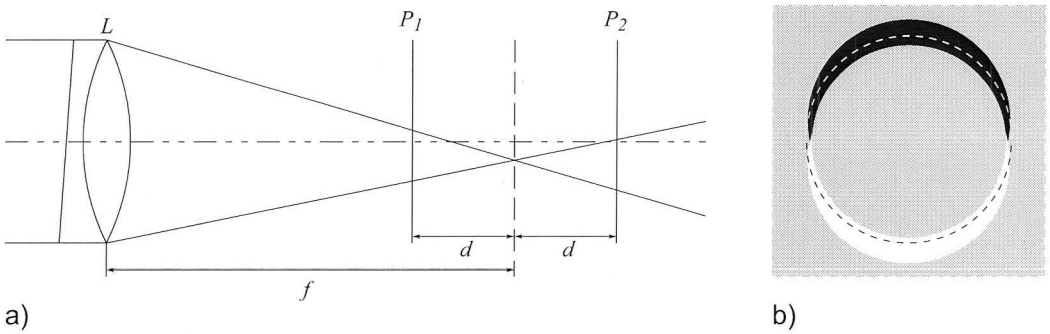

Figure 3.1: Operation of a curvature sensor. a) A tilted wavefront causes different illuminations in planes P_1 and P_2. The normalized difference is shown in b) where white is positive, gray is zero, and black is negative.

and $\nabla^2 z$ is the wavefront curvature.

The distance d must be chosen such that the blur of the pupil image in P_1, $\lambda(f-d)/r_0$, is small compared to the size of fluctuations to be measured, $r_0\frac{d}{f}$. In closed loop AO operation, the blur is reduced and the distance d can be reduced to increase sensitivity.

The curvature sensor is particularly well suited for operation with bimorph and membrane type deformable mirrors. As described in Section 4.1.2, both of these mirrors have transfer functions that solve the Poisson equation.

3.1.2 Shack-Hartmann Sensor

The Shack-Hartmann sensor is a modification of the Hartmann mask technique for measuring optical qualities. Figure 3.2 illustrates the operation of such a wavefront sensor. A sheet of micro-lenses, termed a lenslet array, is placed in a plane conjugate to the pupil. Each lenslet is a subaparture, intercepting the light from a segment of the full pupil image, and forms an image of the source at the lenslet focal plane. Wavefront tilt across a lenslet subaperture will cause the focussed spot to displace an amount proportional to thc local wavefront slope.

A four cell detector, or quad-cell, is placed at the image of each lenslet as in Figure 3.3a. With a reference plane wave, the light intensity will, ideally, be equal in each quadrant. When the spot is displaced by an aberrated wavefront, the centroid position in x and y coordinates can be determined from the reported intensities. In Figure 3.3b, the signal from

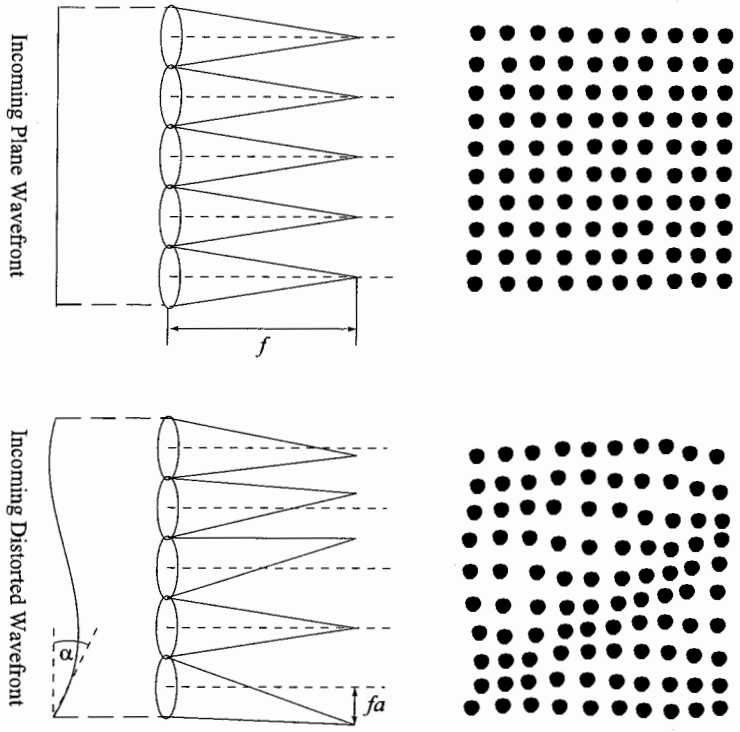

Figure 3.2: The theory of operation of a Shack-Hartmann wavefront sensor. a) A plane wave creates a regular grid of spots, b) an aberrated wavefront displaces spots proportional to local wavefront slope.

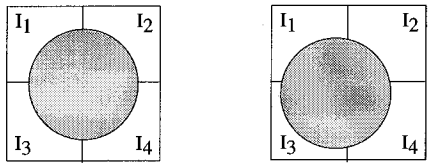

Figure 3.3: Quad-cell detector in a Shack-Hartmann wavefront sensor.

I_3 is increased while that from the other three quadrants is reduced. Centroid estimation can be accomplished using a centre of gravity calculation:

$$c_x = \frac{\sum_{i,j} x_{i,j} I_{i,j}}{\sum_{i,j} I_{i,j}} \quad \text{and} \quad c_y = \frac{\sum_{i,j} y_{i,j} I_{i,j}}{\sum_{i,j} I_{i,j}}. \tag{3.2}$$

Kasper et al. determined that a more accurate centroid is recorded when the pixel intensity is weighted by the photon noise [24]:

$$c_x = \frac{\sum_{i,j} x_{i,j} (I_{i,j})^{1.5}}{\sum_{i,j} (I_{i,j})^{1.5}} \quad \text{and} \quad c_y = \frac{\sum_{i,j} y_{i,j} (I_{i,j})^{1.5}}{\sum_{i,j} (I_{i,j})^{1.5}}. \tag{3.3}$$

With the advent of high quantum efficiency and low noise CCD cameras, they have become desirable for use as the detector in the lenslet focal plane. One can achieve negligible interpixel gap and read out the entire array of spot data simultaneously.

3.2 Test-Bed Wavefront Sensor Design

Due to the relative ease of implementation and ability to reconfigure the lenslet array to accomodate different situations, a Shack-Hartmann wavefront sensor was chosen for the adaptive optics testbed.

3.2.1 Camera

Two principle criteria govern the selection of a CCD camera for use as the wavefront sensor in an adaptive optics system. First, the camera must operate at frame rates high enough

to adequately sample the temporal variations of turbulence the AO system is to correct. Second, the CCD resolution must be such that accurate centroids may be calculated for each lenslet sub-aperture.

The camera selected for this application was the Dalsa CA-D1-0128A-R01M digital camera. With a frame rate of 736 fps this camera is quite well suited for sampling high frequency atmospheric turbulence. The 128 x 128 pixel resolution is sufficient for calculating centroids of up to 32 x 32 sub-apertures (assuming quad cells and 2 pixels dead space between each sub-aperture). The pixel dimensions are 16 μm $\times$ 16 μm. The total sensor dimensions are 2.1 mm by 2.1 mm. The small CCD will require demagnifying optics to image currently available corrective elements. The camera readout uses an 8-bit analog to digital converter with a specified noise level of 1.9 digital numbers (DN). The dynamic range and noise levels of the camera are insufficient for low-light work but are acceptable in a laboratory environment where light intensity is not a problem.

3.2.2 Lenslet Array

The selection of the lenslet array is a balancing act between a number of considerations.

1. Adequate sampling of the wavefront for the number of degress of freedom to be controlled.

2. Light gathering and imaging efficiency.

3. Range of spot motion for expected turbulence.

The number of lenslets across the WFS aperture needs to be at least half as many as there are actuators projected across the aperture (for zonal control). If this were not the case then the control system would be underdetermined with a larger number of degrees of freedom than measurements (there are two slope measurements per lenslet subaperture). Ideally, the number of lenslets across the pupil image is an integer multiple of the number of actuators of the corrective element projected on the pupil. This criterion helps to define the lenslet diameter or pitch.

However, the more lenslets there are across the aperture the less light each lenslet subaperture will collect and focus on the CCD. The diameter and focal length of the lenslets will

also affect the size of an individual spot on the CCD. Assuming a circular lenslet aperture (a reasonable approximation in most cases), the diameter of the focused spot to the first dark ring of the diffraction pattern (the Airy disc) is given by

$$d_{spot} = 2.44\frac{\lambda f}{d_{lenslet}}, \tag{3.4}$$

where f is the lenslet focal length and λ the wavelength of light.

Demagnification of the optical system will amplify the angular range over which the spot will move for a given tilt imparted by turbulence as described by the Lagrange invariant in the paraxial approximation:

$$nh\alpha = n'h'\alpha', \tag{3.5}$$

where n is the index of refraction, h is the object height and α the angle of incidence. The unprimed quantities indicate object space and the primed quantities indicate image space.

Finally, the angle of arrival of light at the lenslet array and the lenslet focal length will determine the extent of motion of a spot on the CCD based on the simple relation $\Delta r = f\alpha'$. It is essential that spots are not able to wander into adjacent cells ($\approx 1/2d_{lenslet}$) under the anticipated turbulence of the system.

To determine the extent of the spot motions on the CCD a statistical measure of the tilt caused by turbulence must be considered. Tatarskii showed that the variance of the angle of arrival of light for a circular aperture D is given by [41]

$$\left\langle \alpha_x^2 \right\rangle = 2.91 D^{-1/3} \sec\gamma \int_0^\infty C_N^2(h)\mathrm{d}h, \tag{3.6}$$

where γ is the zenith angle and C_N^2 is the atmospheric refractive index structure constant (dependent on height). Using the formal definition of r_0 given by [12],

$$r_0 = \left[0.423k^2 \left(\sec\gamma\right) \int C_N^2(h)\mathrm{d}h\right]^{-3/5}, \tag{3.7}$$

where k is the wave-number $2\pi/\lambda$, we can substitute Equation 3.7 in Equation 3.6 and after a simple manipulation, achieve

$$\langle \alpha_x^2 \rangle = \frac{6.88}{4\pi^2} \left(\frac{\lambda}{D}\right)^2 \left(\frac{D}{r_0}\right)^{5/3}. \tag{3.8}$$

It is worth noting that $\langle \alpha_x^2 \rangle$ does not depend on wavelength due to the $\lambda^{6/5}$ term in the definition of r_0.

Making use of the design specification for $D/r_0 = 10.0$, $D = 22$ mm, and $\lambda = 633$ nm then $\langle \alpha_x^2 \rangle = \sigma_\alpha^2 = 6.62 \times 10^{-9}$ rad^2.

Assuming a normal distribution of tilt in which 99.7% of the values lie within three standard deviations of the mean we can expect the range of tilt to be less than

$$3\sigma_\alpha = \alpha_{turb} = 2.44 \times 10^{-4} \text{ rad} \tag{3.9}$$

most of the time. However, the beam diameter at the lenslet array is only 2.1 mm. Since the refractive medium is the same (air) at the turbulence and the lenslet array, those terms cancel from Equation 3.5 and we are left with $h\theta = h'\theta'$. Recalling that the clear aperture of the demagnification lenses in the optical design of Section 2.3.1 is 22 mm and substituting Equation 3.9 for θ, the tilt angle due to turbulence at the WFS will be $\theta' = (h/h')\theta = 2.56$ mrad.

Based on the criteria described above, Table 3.1 summarizes the characteristics of a number of lenslet arrays available from Adaptive Optics Associates. The S in the model numbers indicates the lenslets are in a square configuration. This is ideal for proper registration of the actuators from the selected deformable mirror to the lenslet subapertures. The pixel dimensions assume a 16 μm pixel size.

All of the lenslet arrays are compatible with the magnitude of turbulence (no spot displaces outside it's subaperture). However, only the first two models and marginally the third provide adequate sampling for controlling a 10×10 system of actuators when used with the 2.1 mm Dalsa CCD. Since a circular pupil ten actuators across was to be controlled (see Figure 5.2), the 0188-8.0-S lenslet was selected. The optical design presented in Section 2.3

Model #	Diameter (μm)	f Length (mm)	Pixels per Subaperture	Spot Diameter (μm)	Spot Diameter (pixels)	Spot Motion (μm)	Spot Motion (pixels)
0188-8.0-S	188	8.0	11.75	65.7	4.11	20.4	1.28
0190-10-S	190	10.0	11.875	81.3	5.08	25.6	1.60
0200-6.3-S	200	6.3	12.5	48.6	3.04	16.1	1.01
0250-18-S	250	18.0	15.625	111.2	6.95	46.0	2.88
0250-19-S	250	19.0	15.625	117.3	7.33	48.6	3.04
0312.5-34-S	312.5	34.0	19.53	168.0	10.5	86.9	5.43

Table 3.1: Lenslet array properties

is optimized for this lenslet array.

3.2.3 Opto-Mechanical Design

The mechanical design requirements for the construction of the Shack-Hartmann wavefront sensor were as follows:

1. Allow interchangeable lenslet arrays.
2. Allow rotation of lenslet array.
3. Allow adjustment of focus without rotating lenslet array.
4. Mount to the camera chassis.

An exploded view of the final design is shown in Figure 3.4. The lenslet array (mounted on a 6 mm thick BK7 glass substrate) rests on a flange at the base of the lenslet retention barrel. A Delron cylinder (not shown) with an axially compressed O-ring in the base is press-fit in the lenslet retention barrel to fix the lenslet array in place. This cylinder can be rotated, and due to the O-ring friction, will rotate the lenslet array to allow adjustment of the orientation. A separate lenslet retention barrel was manufactured for each lenslet focal length with the flange depth adjusted to place the lenslet array at its nominal focus from the camera CCD.

The lenslet retention barrel slides inside the translation barrel. The translation barrel is threaded and screws into the camera housing. The threading allows up to ± 2.5 mm of travel about the mid-point to fine tune the lenslet focus on the CCD. The lenslet retention barrel remains flush against the translation barrel due to a pair of tensioning springs attached

between the pegs at the front of the rentention barrel and the Z-axis aligner. The Z-axis aligner bolts directly to the camera housing and fits snugly about the translation barrel, providing the rigidity required to maintain the lenslet to CCD alignment.

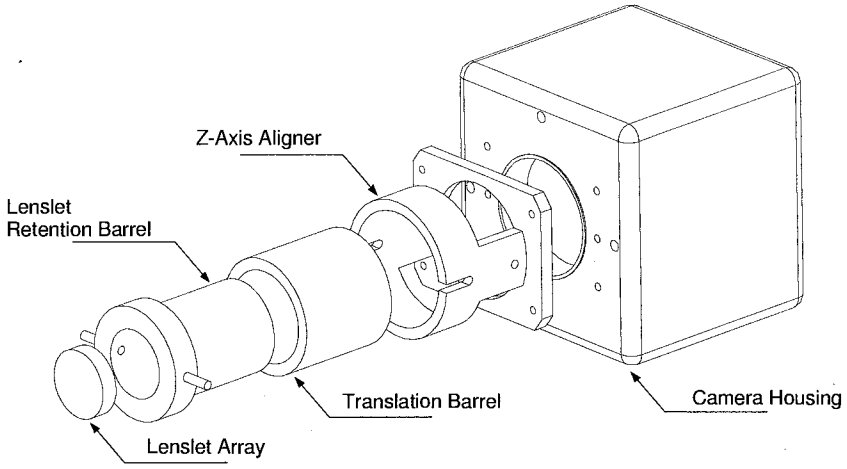

Figure 3.4: Exploded view of Shack-Hartmann wavefront sensor.

3.2.4 Computer Interface and Software

The computer operating system platform selected to control the AO test bench was QNX 4.25. The QNX OS offers hard real-time performance and a configurable micro-kernel.

Data flow from the camera to the computer, including the pre-processing steps prior to the AO controller itself, is shown schematically in Figure 3.5. The Dalsa digital camera is connected to a Bitflow RUN-PCI-11 Roadrunner single tap, 8-bit digital camera frame grabber. The frame grabber supplies the clock signals to the camera to control frame rate and exposure time and also reads the camera CCD image. The frame grabber is capable of direct memory access (DMA) transfer of image data to place the image directly into computer memory, bypassing the CPU and reducing processing overhead. The QNX device driver for the frame grabber was provided by Quality Real-Time Systems (QRTS).

During initialization of the control system, a CCD background noise level is determined. This is generally 11-13 digital counts from ambient lighting. The background level is subtracted from all pixels and any resultant negative values are set to zero for all subsequent

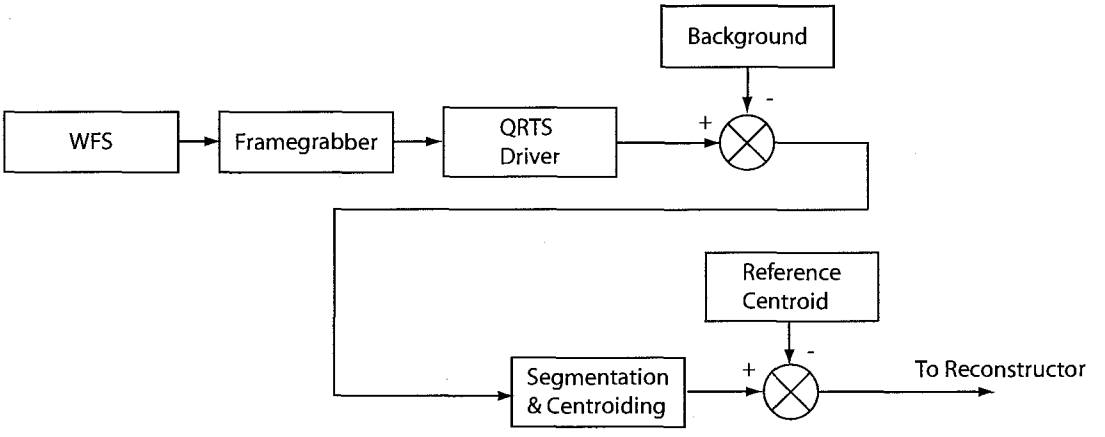

Figure 3.5: Wavefront sensor data flow chart.

frames captured. This step helps improve the accuracy of the centroid algorithms of Equation 3.2 and reduce noise propagation through the controller.

Another intialization step for configuring the wavefront sensor is segmenting the CCD into cells in which spots will be found. To achieve this, a reference image from the WFS is acquired. This is an image of the sub-aperture spot positions in the absence of turbulence, with the tip-tilt mirror at its mid position, and with a $\lambda/20$ flat mirror used in place of the DM. The pixel locations of four corner spots, the number of spots in x and y directions, and the 'radius' of a bounding box about a spot are identified. These parameters define a cell grid, each cell contains one spot and has dimensions such that it does not overlap with a neighbouring cell and the spot will not travel outside the cell under the influence of turbulence.

The centroid location for each spot is calculated using only the pixels contained in that spot's corresponding cell. The centroids from the reference image establish a home position that the control system will attempt to achieve when operating in closed loop with the DM and tip-tilt mirrors. The centroid positions from the reference image are subtracted from those measured in real-time in closed loop, giving a relative displacement from the home position. A vector of spot displacements is then passed to the controller, further described in Chapter 5.

Chapter 4

Deformable Mirrors

The goal of an adaptive optics system is to compensate for the wavefront distortions caused by the propagation medium (atmosphere etc). Phase fluctuations are predominant thus an AO system must include a device capable of introducing a phase shift. These devices produce an optical phase shift, ϕ, by varying the optical path difference, δ.

$$\phi = \frac{2\pi}{\lambda}\delta \tag{4.1}$$

The path difference $\delta = \Delta(ne)$ is the variation of the optical path ne where n is the index of refraction and e is the geometrical path length. A transmissive device such as a liquid crystal spatial light modulator achieves the phase shift by varying the refractive index. However, a deformable mirror (DM) is generally preferred due to faster response times and wavelength independence. Such devices vary the geometrical path length by physically deforming a reflective surface, changing e.

4.1 Deformable Mirror Review

4.1.1 Segmented Mirror

The segmented mirror consists of a number of discrete mirror segments, each individually controlled. If an elementary mirror is driven by a single actuator as in Figure 4.1a, the motion is limited to piston only. By utilizing three actuators per segment, piston and

tip/tilt can be controlled as in Figure 4.1b, resulting in much lower fitting error.

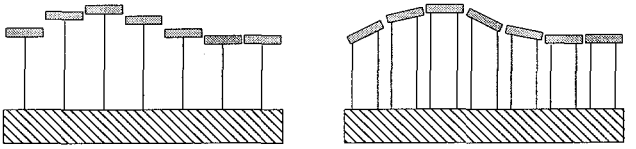

Figure 4.1: Segmented mirror types.

An advantage to the segmented mirror is that it scales well, 500 element mirrors have been demonstrated [20]. Another potential advantage is that failures are easily repaired, though not in a micro scale mirror.

The most significant disadvantage of the segmented mirror is the high fitting error and diffraction effects at gaps between segments. Hudgin showed that approximately six times more piston mirrors are required to achieve the same fitting error as a continuous facesheet mirror with a gaussian actuator influence function [18]. Piston and tip/tilt control reduces the required number of segments to 4/3 the number of actuators of a continuous mirror, but there are three times as many actuators per segment.

4.1.2 Continuous Mirrors

Due to their lower wavefront fitting error and reduced number of required actuators to achieve this, the continuous facesheet deformable mirror is usually preferred in AO systems. A number of different continuous mirror strategies have been developed including monolithic and discrete stacked piezoelectric, bimorph, and membrane mirrors.

Monolithic Piezoelectric Mirror

The monolithic piezoelectric mirror (MPM) was developed to address stability and thermal distortions of discrete piezoelectric actuator mirrors [10, 19]. An MPM was one of the first deformable mirrors to be employed in an AO system [17]. A schematic MPM is shown in Figure 4.2. The mirror consists of a monolithic block of piezoelectric material. An array of electrodes is placed at the top surface. Each electrode is addressable via a wire passing through the block. A common electrode is attached to the back of the block.

An aluminized thin glass mirror is attached to the top surface. The mirror is actuated by selectively applying bipolar voltages to the electrodes with respect to the common electrode.

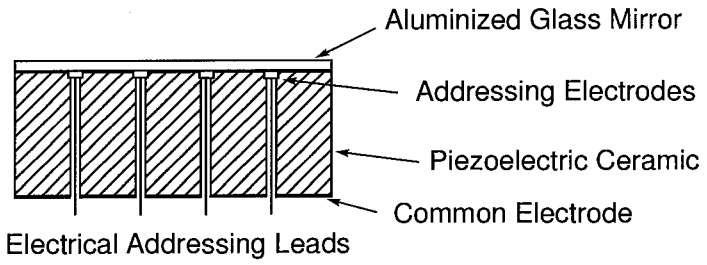

Figure 4.2: Monolithic piezoelectric mirror

Bimorph Mirror

The operation of the bimorph mirror is based upon the flexural response of a piezoceramic due to an applied electric field. A single actuator unimorph design was described by Adelman in 1977 for controlling the curvature of a mirror with negligible deviation from sphericity [1]. Since then a number of designs with increasing number of actuators have been constructed [8, 11, 27, 40].

The bimorph design is illustrated in Figure 4.3. Two thin, oppositely polarized piezoceramic plates are sandwiched together about a common electrode. An electrode pattern is deposited on the outer surfaces of the plates. When a voltage is applied, one plate expands and the other contracts, causing a local bending about the electrode. A thin glass plate is typically bonded to the piezoceramic to provide an optical quality reflecting surface.

The transfer function of an ideal bimorph mirror has the form [37]:

$$\frac{\partial^2 Z}{\partial t^2} = A\nabla^4 Z + B\nabla^2 V, \tag{4.2}$$

where Z is the surface displacement, A and B are constants, and V is the voltage distribution on the piezoelectric plates.

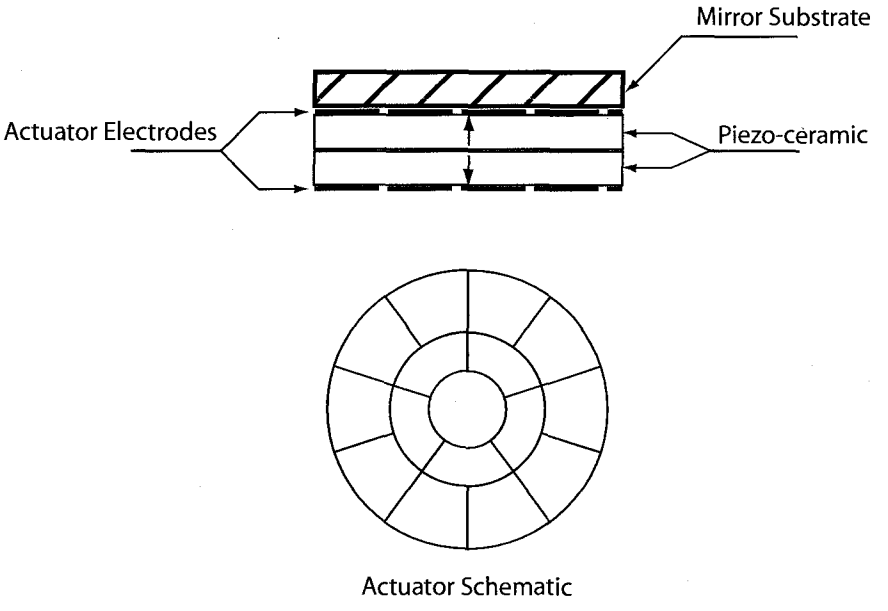

Figure 4.3: Bimorph mirror schematic and typical electrode pattern.

Membrane Mirror

The membrane mirror is an electrostatically actuated thin film mirror. The membrane mirror has been demonstrated in many AO applications [7, 33, 44, 47, 50]. It consists of a grounded metallized membrane suspended under tension between a transparent electrode and a region of actuators as illustrated in Figure 4.4. The transparent electrode carries a bias voltage V_0 while the actuator pads have a voltage $V_0 \pm \Delta V$. Actuators are typically organized in a hexagonal pattern.

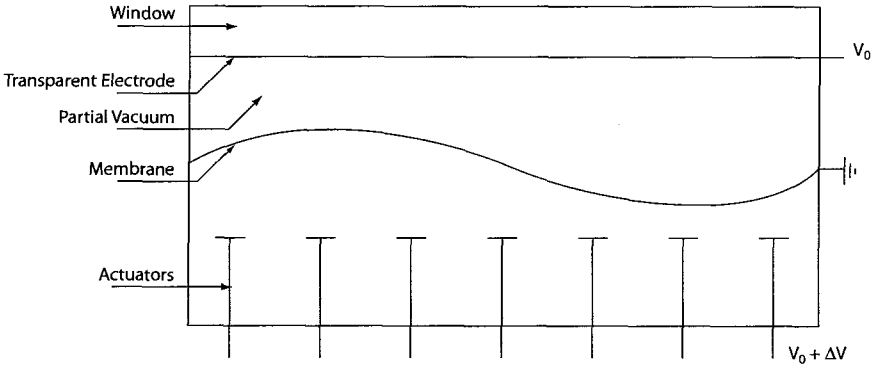

Figure 4.4: Membrane mirror schematic.

The transfer function of a membrane mirror under an external force $F(\boldsymbol{r}, t)$ is given by [15]:

$$\frac{\partial^2 Z}{\partial t^2} = \frac{T}{\sigma}\nabla^2 Z + \frac{F(\boldsymbol{r}, t)}{\sigma}, \tag{4.3}$$

where Z is the vertical displacement, t is time, T is the tension per unit length, and σ is the mass per unit area.

Advantages to the membrane mirror design are no hysteresis, low voltage operation and high resonant frequency.

4.2 MEMS Deformable Mirror

Micro Electromechanical Systems (MEMS) refers to a manufacturing process rather than a specific design. The manufacturing process generally involves bulk silicon machining. The advantages to this technique are the low cost per actuator and the potential scalability to DM systems with thousands of actuators. MEMS based mirrors have been proposed for next generation telescope AO systems requiring up to one hundred thousand actuators [49]. Both continuous and segmented MEMS mirrors have been fabricated [46].

The MEMS mirror selected for operation with the AO testbed was manufactured by Boston Micromachines (BM). The device was constructed using a six-layer thin film conventional silicon micromachining process. A schematic of the mirror is shown in Figure 4.5. The thin film layers (from bottom to top) are [4]:

1. Low-stress chemically vapour deposited (CVD) 0.5 μm silicon nitride film providing isolation between substrated and the device.

2. CVD 0.5 μm silicon film for the bottom actuator electrode.

3. CVD 5.0 μm silicon dioxide sacrificial layer to define the actuator air gap.

4. CVD 2.0 μm silicon film for the bendable actuator electrode.

5. CVD 2.5 μm silicon dioxide sacrificial layer defining the space between the actuators and the mirror.

6. CVD 3.0 μm silicon film used as the mirror surface and attachment posts between actuators and the mirror surface.

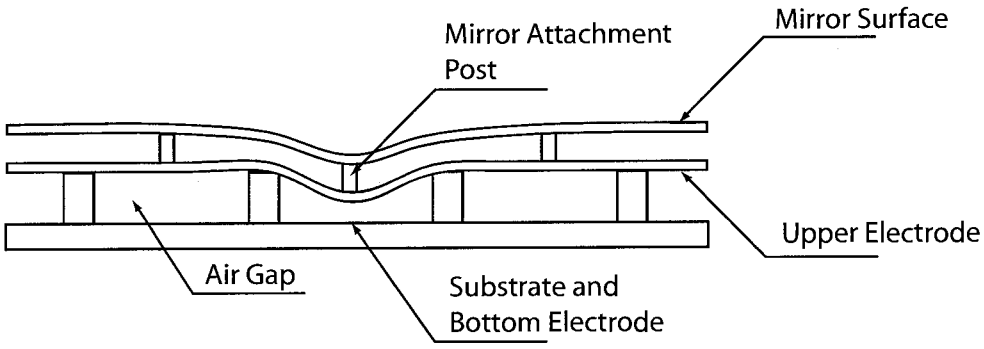

Figure 4.5: Boston Micromachines DM schematic (not to scale).

The actuator membrane (layer 4) serves as the upper electrode of a parallel plate capacitor. The stationary layer (layer 2) serves as the second electrode of the capacitor. When a voltage difference is applied between the lower electrode and grounded upper electrode, the actuator membrane deflects downwards. The attachment post and mirror surface are correspondingly deflected.

Excessive interactuator curvature due to residual strain in the silicon was reduced by bombardment by neutral ion beams [3]. Additionally, roughness of the silicon mirror surface was reduced to 12 nm using a chemo-mechanical polishing process [35]. Lastly, an approximately 50 nm thick gold coating was deposited on the mirror surface after release to improve reflectivity while avoiding the addition of high tensile stresses.

The DM itself is in a square format 3.3 mm to a side. The actuator layout is a square grid of 12 $\times$ 12 actuators, missing the corners, for a total of 140 actuators. Actuators are on a 300 μm grid spacing. The mirror surface is a hybrid design with cuts to the mirror face over the attachment points. This design was developed as a means to reduce inter-actuator coupling to approximately 10% while also limiting the diffraction effects of a segmented mirror [5]. A summary of the mechanical properties of the BM DM can be found in Table 4.1.

Clear Aperture	3.3 mm
Number of Actuators	140
Actuator Configuration	12×12 (without corners)
Flatness (unpowered)	< 30 nm RMS
Reflectivity	$> 98\%$ (@633 nm)
Actuator Spacing	300 μm
Inter-Actuator Coupling	15%
Stroke	2 μm
Hysteresis	0%
Lifetime	>1B cycles @ 1/2 stroke
Open-loop bandwidth	DC 6.6 kHz (in air)

Table 4.1: BM DM mechanical properties.

4.2.1 Bending Theory

The capacitive design of the DM actuator can be modelled as a simply supported rectangular thin plate under a uniform load. The partial differential equation governing the deflection of a thin plate is [42]:

$$\nabla^4 w = \frac{\partial^4 w}{\partial x^4} + 2\frac{\partial^4 w}{\partial x^2 \partial y^2} + \frac{\partial^4 w}{\partial y^4} = \frac{q}{D}, \tag{4.4}$$

where w is the plate displacement, q is the load and D is the flexural rigidity of the plate, given by:

$$D = \frac{Et^3}{12(1-\nu^2)}, \tag{4.5}$$

where E is the modulus of elasticity and ν is Poisson's ratio of the material, in this case, silicon.

Using the Navier solution method to solve Equation 4.4 in which the load is represented by a Fourier series:

$$q(x,y) = \sum_{m=1}^{\infty}\sum_{n=1}^{\infty} a_{mn} \sin\frac{m\pi x}{L_x} \sin\frac{n\pi y}{L_y}, \tag{4.6}$$

yields a solution of the form [42]:

$$w(x,y) = \frac{1}{\pi^4 D}\sum_{m=1}^{\infty}\sum_{n=1}^{\infty} \frac{a_{mn}}{\left(\frac{m^2}{L_x^2} + \frac{n^2}{L_y^2}\right)^2} \sin\frac{m\pi x}{L_x} \sin\frac{n\pi y}{L_y}, \tag{4.7}$$

where a_{mn} is a coefficient determined by the load distribution on the plate. For the case of

a uniformly distributed load [42]:

$$a_{mn} = \frac{4q_0}{L_x L_y} \int_0^{L_x} \int_0^{L_y} \sin\frac{m\pi x}{L_x} \sin\frac{n\pi y}{L_y} dxdy = \frac{16q_0}{\pi^2 mn}, \tag{4.8}$$

giving

$$w(x,y) = \frac{16q_0}{\pi^6 D} \sum_{m=1}^{\infty} \sum_{n=1}^{\infty} \frac{\sin\frac{m\pi x}{L_x} \sin\frac{n\pi y}{L_y}}{mn\left(\frac{m^2}{L_x^2} + \frac{n^2}{L_y^2}\right)^2} \tag{4.9}$$

The load, q_0, is generated by the electrostatic attractive force between the capacitive plates. The energy stored in a capacitor is given by the formula:

$$U = \frac{1}{2}\epsilon_r \epsilon_0 A \frac{V^2}{z}, \tag{4.10}$$

where ϵ_r is the dielectric constant (approx. 1 for air), ϵ_0 is the vacuum permittivity ($8.854 \times 10^{-12}\ Fm^{-1}$), A is the plate area, V is the applied voltage and z is the separation of the plates.

The force on the bendable electrode is given by

$$F = -\frac{\partial U}{\partial z} = \frac{\epsilon_r \epsilon_0 A}{2} \frac{V^2}{z^2}. \tag{4.11}$$

Thus the load on the bendable plate is

$$q_0 = \frac{\epsilon_r \epsilon_0}{2} \frac{V^2}{z^2}. \tag{4.12}$$

Substituting this into Equation 4.9 we can see that the displacement is proportional to the square of the voltage applied.

Chapter 5

Control System

The control system for an adaptive optics system is responsible for interpreting the WFS data and determining what adjustments need to be made to the corrector(s) to reduce the aberrations present in the light path. A principal goal of the AO test-bed control system design was to provide a structure in which different hardware could be employed and control schemes evaluated.

The block diagram in Figure 5.1 illustrates the control system of the AO test bed. The portion surrounded by the dotted line, relating specifically to the wavefront sensor, has previously been described in detail in Section 3.2.4 and will briefly be summarized here. The gray blocks are control elements specific to the modal controller.

Segmentation & Spot Position

During the initial setup for closed loop AO operation a reference image from the WFS is acquired. This is an image of the sub-aperture spot positions in the absence of turbulence, with the tip-tilt mirror at its mid position, and with a $\lambda/20$ flat mirror used in place of the DM. This establishes a home position that the control system will attempt to achieve when operating in closed loop with the DM.

A grid of pixel bounding boxes is established such that each reference spot is nominally centered in a box and no two boxes overlap. This segmentation of the CCD is used in closed loop operation for determining the pixels to use for the centroid calculation of each spot

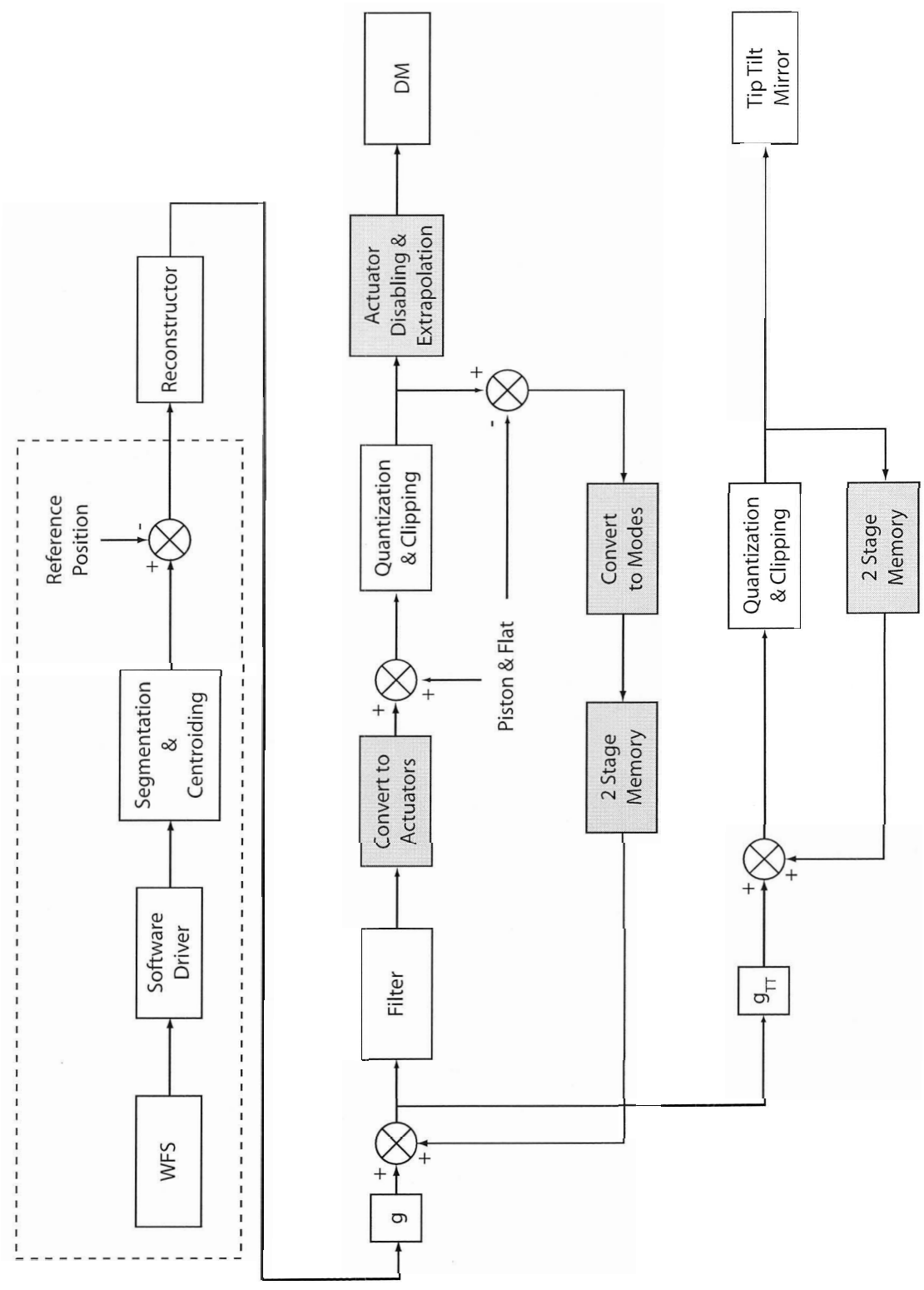

Figure 5.1: Control system of the adaptive optics test-bed. Grayed items are specific to the modal controller.

(Equation 3.3).

The centroid positions from the reference image are subtracted from those calculated during closed loop operation to give a relative change of slope from the desired home position.

5.1 Reconstructor

The reconstructor is a matrix relating the actuator error signals to slopes (or equivalently, spot displacements). During system calibration, a relationship is established between slopes and actuators for known displacements. This relationship can be represented in matrix notation as

$$\mathbf{s} = \mathbf{A}\phi, \tag{5.1}$$

where $\mathbf{s}$ is a column vector of $2(n-1)^2$ slope measurements, $\mathbf{A}$ is a $2(n-1)^2 \times n^2$ matrix referred to as the interaction matrix and ϕ is a column vector of n^2 actuator displacements in microns (assuming an $n \times n$ controlled square of actuators). The dimensions of these matrices are determined by the geometry of the system as shown in Figure 2.5.

During closed loop operation we wish to reconstruct actuator displacements from measured spot displacements. To accomplish this, the inverse of Equation 5.1 must be solved

$$\phi = \mathbf{A}^{\dagger}\mathbf{s}. \tag{5.2}$$

Here, $\mathbf{A}^{\dagger}$ indicates a generalized matrix inverse. $\mathbf{A}$, a typically non-square matrix, is inverted using singular value decomposition (SVD) to give a reconstruction matrix (or reconstructor).

The SVD theorem states that there exists a product of matrices such that

$$\mathbf{A} = \mathbf{U}\mathbf{\Sigma}\mathbf{V}^{\mathbf{T}}, \tag{5.3}$$

where $\mathbf{U}$ and $\mathbf{V}$ are orthogonal, and $\mathbf{\Sigma}$ is a diagonal matrix of singular values. The SVD has the effect of generating an orthogonal set of operating modes (the $\mathbf{V}$ matrix) from

the interaction matrix such that the corresponding wavefront sensor measurements are also orthogonal (the **U** matrix). The singular values represent the sensitivity of the system to the eigenmodes.

The rows of the **V** matrix correspond to the actuators or basis modes poked when forming the interaction matrix. The columns of the **V** matrix represent linear combinations of the actuators or modes to form the orthogonal set of eigenmodes of the system.

The reconstructor, $\mathbf{A}^{\dagger}$ is formed easily by utilising the properties of the orthogonal matrices:

$$\mathbf{A}^{\dagger} = \mathbf{V}\mathbf{\Sigma}^{-1}\mathbf{U}^{\mathbf{T}}. \tag{5.4}$$

Since $\mathbf{\Sigma}$ is diagonal, its inverse is simply the numerical inverse of the diagonal elements. A threshold may be set on the singular values, forcing the inverse of small values to zero, and is generally necessary to eliminate hidden modes such as waffle during DM operation. In closed loop operation, the vector of spot displacements is multiplied by the reconstructor matrix giving a vector of actuator errors. The actuator errors are integrated. Two forms of reconstructor are currently available: zonal and modal.

5.1.1 Zonal Reconstructor

For a zonal reconstructor, the interaction matrix, **A**, is constructed by separately poking each actuator a known amount. For each actuator, a vector containing the x and y displacements of every spot during the poke is stored. These vectors form the columns of the interaction matrix.

Due to the relatively large influence function (see Section 6.2.3) of an actuator, a single actuator influences up to twelve spots. However, this still leaves the interaction matrix quite sparse. Typically, a spot displacement is only considered significant if its magnitude exceeds a specified threshold; all other values are clamped to zero. This is used to reduce the impact of noise in the interaction matrix.

A limitation to the zonal reconstructor is that it assumes when multiple actuators are poked simultaneously, that the combined influence function is a superposition of the individual influence functions. This assumption is incorrect for the BM DM used, particularly

in the region between displaced actuators as will be illustrated in Section 6.2.3.

5.1.2 Modal Reconstructor

The modal reconstructor takes a different approach when forming the interaction matrix. Instead of poking individual actuators, a set of orthogonal surface shapes are applied. The Zernike polynomials defined by Noll [32] are frequently used as a modal basis. However, since Zernike polynomials are defined on polar coordinates, they are not ideally suited for the rectangular grid of the BM DM actuators. Instead, a basis of rectangular polynomials as defined by Table 5.1 was used. The matched coordinate system allows for a higher spatial frequency to be represented on the mirror without aliasing.

	x	x^2	x^3	$\cdots$	x^n
y	xy	x^2y	x^3y		
y^2	xy^2	x^2y^2	x^3y^2		
y^3	xy^3	x^2y^3	x^3y^3		
$\vdots$				$\ddots$	
y^n					x^ny^n

Table 5.1: Orthogonal modal basis functions defined on a rectangular grid (from Hampton [16])

The modal approach to the reconstructor ensures that the controller has an accurate knowledge of the surface shape the DM is taking.

Filter

A configurable filter can be used as a form of prediction in the controller. The zonal controller passes the actuator commands without filtering, whereas the tested modal controller uses an equally weighted average of the previous and currently sampled errors. Different weighting schemes or higher order filtering are easily implemented.

Conversion to Actuators

The modal controller must convert from modal error signals to actuator error signals. Following this, a piston value for the actuators is applied to operate the DM about the midpoint

of its displacement. At the same time a fixed shape can also be applied to flatten the mirror to compensate any static aberrations of the optical system. The flat state is determined during calibration in the absence of turbulence with respect to the reference mirror.

The piston and flat state are removed from the feedback path to prevent accumulation of this external input.

Quantization & Clipping

Due to the digital nature of the driver electronics for the mirrors, the actuator error signals must be rounded to the discreet values that the drivers can accept. Noise can also be mitigated during this step by requiring an error of more than one quantization level before the value is applied to the actuator.

The control system may request an actuator move beyond its physical or electrical limits. Clipping limits the maximum and minimum control values that are passed to the mirrors. The feedback path ensures that the controller is aware of the altered actuator state.

Actuator Disabling & Extrapolation

Since modal control defines surface shapes for the entire mirror, it is necessary to disable any dead actuators outside of the reconstructor. For zonal control, dead actuators can be disabled by omitting them in the creation of the interaction matrix.

Depending on the optical design or desired operation, it is possible that some actuators may not be illuminated or actively controlled hence not part of the reconstructor. Actuator signals are extrapolated to these 'dark' actuators using a nearest neighbour algorithm. When operating the square MEMS DM, a central circle of 80 actuators were illuminated and controlled while the remaining 60 'unused' actuators are extrapolated as shown in Figure 5.2. Three of the DM actuators were non-functional.

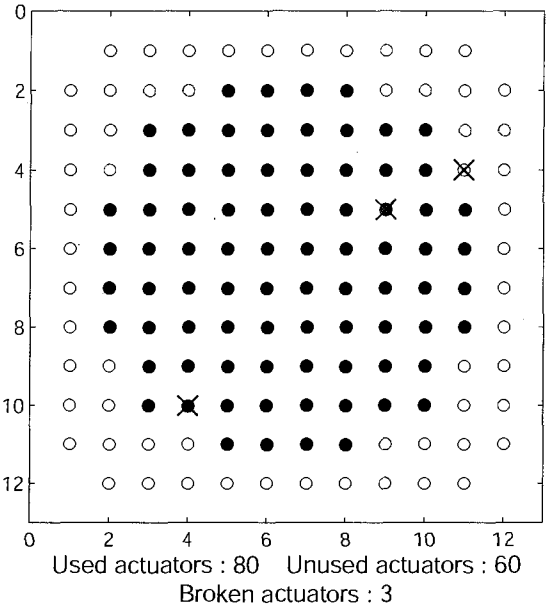

Figure 5.2: DM actuator map, filled circles represent controlled actuators, open circles identify extrapolated actuators, X's indicate dead actuators

Feedback Path

The zonal controller feeds the actuator error minus the piston and flat values back directly. The modal controller requires that actuator errors be converted back to modal error before being fed back. A single integrator is used to accumulate the current actuator state plus the error. Additionally, it was observed that the AO system operates with two delays between outputting an actuator command and observing the effect on the wavefront sensor. A two-stage memory was introduced to feed back the actuator error signal to the corresponding wavefront sensor measurement. The matched delay was not implemented for the zonal controller.

Chapter 6

Results

6.1 Tip-Tilt Mirror Characterization

The operational parameters of interest for the use of a tip-tilt mirror in an AO system are angular range, linearity, and frequency response.

6.1.1 Angular Range and Linearity

The tip-tilt mirror must be capable of correcting the expected maximum magnitude of tilt imparted by turbulence. Making use of Equations 3.5 and 3.9 the maximum tilt due to turbulence at the tip-tilt mirror will be

$$\alpha_{TT} = \frac{d_{turb}}{d_{TT}} \alpha_{turb} = \frac{22.0}{6.6} 2.44 \times 10^{-4} \text{ rad} = 0.813 \text{ mrad}. \tag{6.1}$$

The angular range of the tip-tilt mirror was determined by measuring the displacement of the reflection of a near-normal incidence laser beam on a CCD camera at a known distance from the mirror. The setup was described in Section 2.2. The angular range measured was ± 1.3 mrad on one axis and ± 1.0 mrad on the other. The two axes were oriented at 84.4° to each other. Non-orthogonality does not pose a problem to the control system as it determines a least-squares solution when correcting the phase.

A linear response to input is a desirable property for the control system as it reduces the computations required. Actuator response was linear with respect to the drive voltage

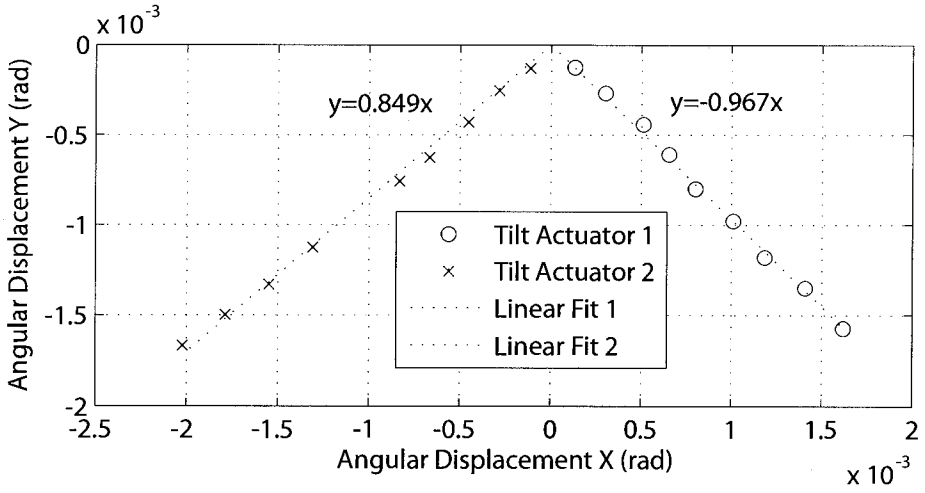

Figure 6.1: Tip-tilt mirror angular displacement of each axis.

as seen in Figure 6.1.

6.1.2 Frequency Response

The frequency response of the tip-tilt mirror was measured using the optical design also described in Section 2.2. The step response of the tip-tilt mirror was found to have strong oscillations at 2.4 kHz, which is the rated resonant frequency of mechanical oscillations. However, the D/A that drives the tip-tilt mirror electronics is not capable of sharp square waves due to a significant slew rate. The tip-tilt response to this slew rate was an angular velocity of 0.5 radians/s up to its intended position, then constant without significant overshoot or oscillations.

6.2 DM Characterization

Surface displacement measurements of the DM were made using a Precision Dynamics PD-1000 fiber optic interferometer (FOI). A schematic of the test setup is shown in Figure 6.2. The interferometer employs a 780 nm stabilized laser diode coupled to a fiber. The fiber terminates in a gradient index (GRIN) lens assembly with a focal length of 7 mm. Interference occurs between the light reflected from the lens front face and the external surface. The interference fringes are tracked at a sampling rate of up to 1 MHz. Subfringe accuracy

is achieved through interpolation, enabling displacement measurements to an accuracy of ± 1 nm. The unit will switch to a low resolution fringe counting mode if the tracking rate is exceeded, in which case the resolution drops to 0.4 μm.

The FOI was mounted on a 3-axis translation stage with micrometer resolution. The fiber tip was positioned approximately 7 mm from the DM surface, the midpoint of distances generating a strong signal as reported by the interferometer. The interferometer was positioned over the peak of an actuator by taking displacement measurements and repositioning until a maximum was found. The fiber was located within ± 1 μm of the peak in both x and y directions.

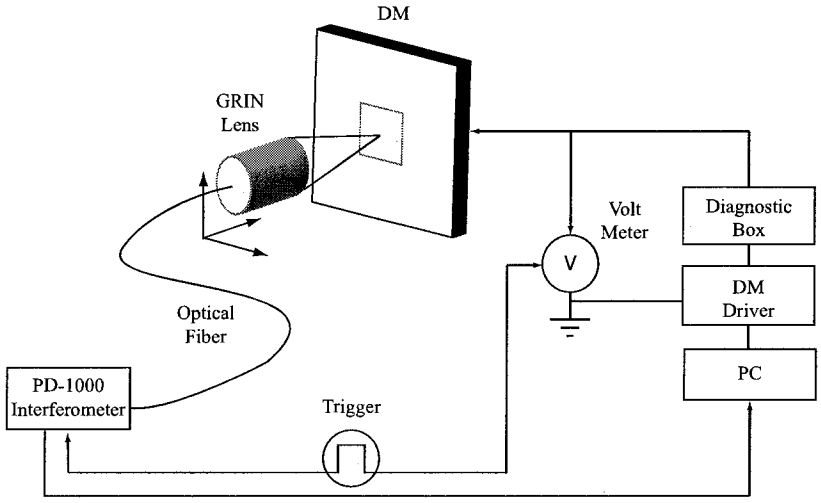

Figure 6.2: Schematic of fiber interferometer setup with DM.

The BM DM was mounted in a tip-tilt mount and clamped to a vibration isolated optical bench. The DM was connected to its 8-bit driver electronics via a diagnostic box. The circuit diagram in Figure 6.3 shows a single channel of the diagnostic box. A resistor divider is used to scale the high-voltage to a 0–10 volt range. The op-amp buffers the signal and provides a safe test point. A diagnostic LED gives visual feedback for the actuator being displaced. All channels were driven to 0 V, except the actuator under test which was driven up to the maximum supply voltage of 185 V.

A National Instruments AT-MIO-16E-10 multi-function data-acquisition card was used to measure the 0–10 V scaling of the DM driver voltage at the test point of Figure 6.3.

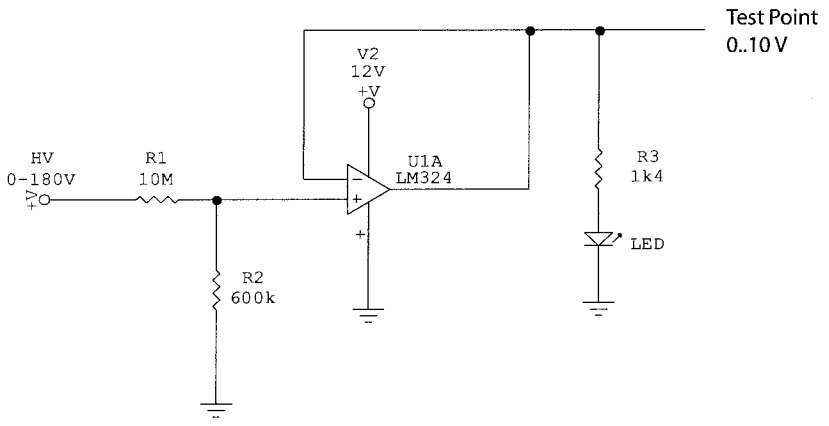

Figure 6.3: Circuit diagram of a single channel of the DM driver diagnostic box.

The voltage sampling rate was set identical to the interferometer sampling rate to have one-to-one correspondence.

An Agilent 33120A function generator was used to produce a square pulse signal to trigger simultaneous acquisition of the voltage and displacement of the DM. The PD-1000 and DAQ card triggered on the falling edge of the square pulse

6.2.1 Stroke and Linearity

Noll [32] derived the residual phase variance after correction of tip and tilt to be:

$$\sigma_\phi^2 = \langle \phi^2 \rangle = 0.134 \left(D/r_0\right)^{5/3}. \tag{6.2}$$

Making use of Equation 4.1, the stroke, δ, required of the DM to correct the residual error 97% of the time for turbulence with $D/r_0 = 10$ at a wavelength of $\lambda = 632.8$ nm is thus

$$\delta = 2 \times \frac{\lambda}{2\pi} 3\sigma_\phi = \frac{3\lambda}{\pi} 0.366 \left(D/r_0\right)^{5/6} = 1.51 \ \mu\text{m}. \tag{6.3}$$

The factor of 2 is required to compensate for $\pm 3\sigma_\phi$. However, the optical path difference is double the physical displacemnt for a reflective device, thus the DM requires a stroke of 0.75 μm to compensate for the maximum expected turbulence.

The Boston Micromachines software interface was used to poke an actuator in single digital number (DN) steps up to the maximum of 255 and return to 0. The applied voltage

and displacement measurements were sampled at identical frequencies.

Figure 6.4 shows the result of one cycle. The maximum displacement observed was 1.080 μm. This was obtained at a DN of 169 indicating that if the power supply were reconfigured, larger displacements might be obtained. Alternatively, a finer resolution within the current stroke, using the full 255 levels of the DAC, could also be achieved with slight modifications. The limited stroke restricts the magnitude of turbulence that can be corrected without saturating the DM.

The negative displacement is an indication that the actuator is moving away from the interferometer since the capacitive actuator plates pull together as voltage is applied. Though not shown to avoid confusion, a quadratic fit of $-3.34E^{-5}V^2+1.86E^{-4}V+3.09E^{-5}$ is nearly indistinguishable. The displacements at identical voltages do differ slightly, however. The voltage supply was confirmed to be repeatable to within a tenth of a volt, suggesting that the mirror exhibits some hysteresis or mechanical effect.

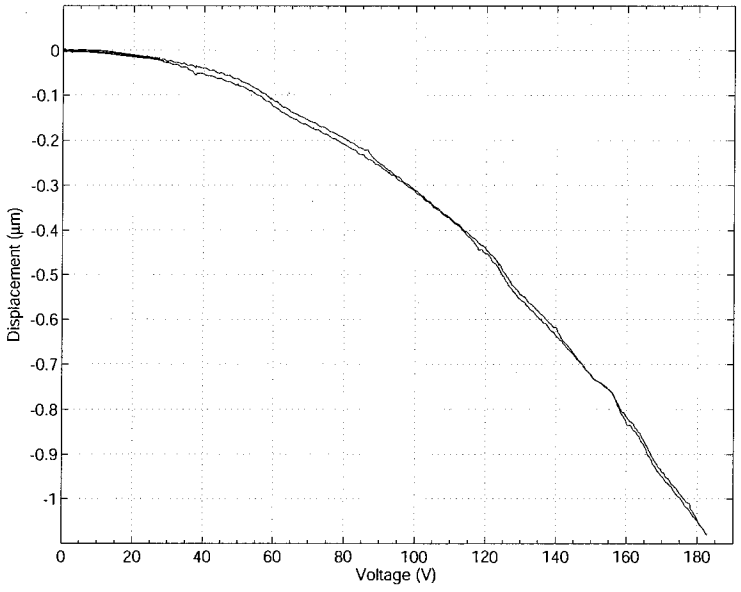

Figure 6.4: DM displacement for an increasing and decreasing voltage cycle.

6.2.2 Response Time

It is important that the response time of the DM actuators to an input be at least as fast as the sampling rate of the AO system. The step response of an actuator was measured at an interferometer sampling rate of 10 kHz. In Figure 6.5 we can see that the time constant (time to reach 63% of displacement), τ, for the actuator is 0.35 ms following a 0.3 ms delay. This appears to be a limitation of the driver electronics since the voltage response has a similar time constant. The steady state is reached in 1.7 ms following the delay.

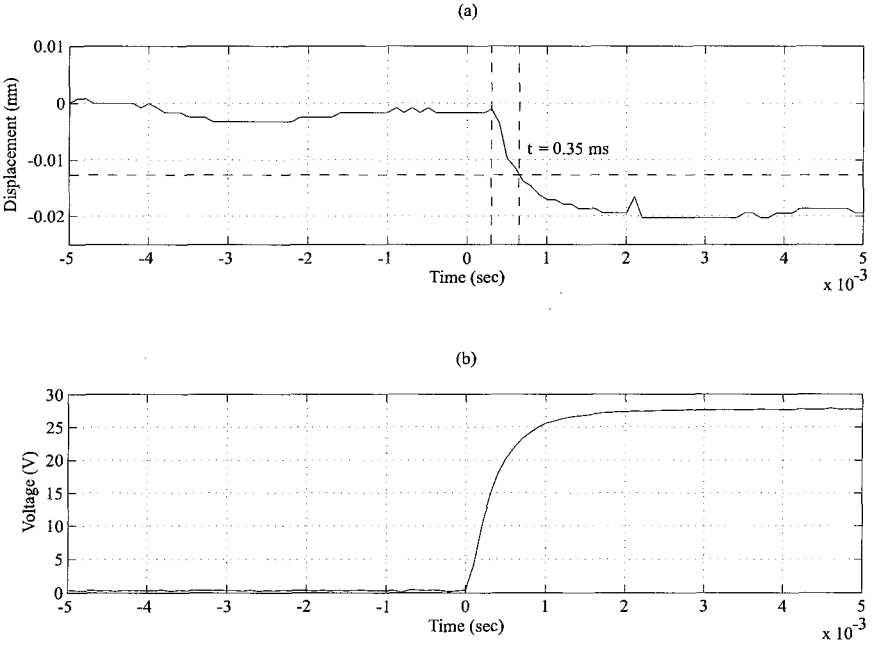

Figure 6.5: (a) DM displacement response time to a (b) voltage step.

6.2.3 Influence Function

The influence function is a displacement map of the DM surface when an actuator is pushed. It is an essential measure for constructing a basis set of control modes in actuator space and is also used in software modeling of the AO sysem. To measure the influence function, a single actuator was poked at 75% of the maximum command voltage. Interferometer sample points were coarsely spaced at 100 μm with 50 μm intervals around the peak and wings of the response. Figure 6.6 shows the FOI results interpolated on a 25 μm grid. The

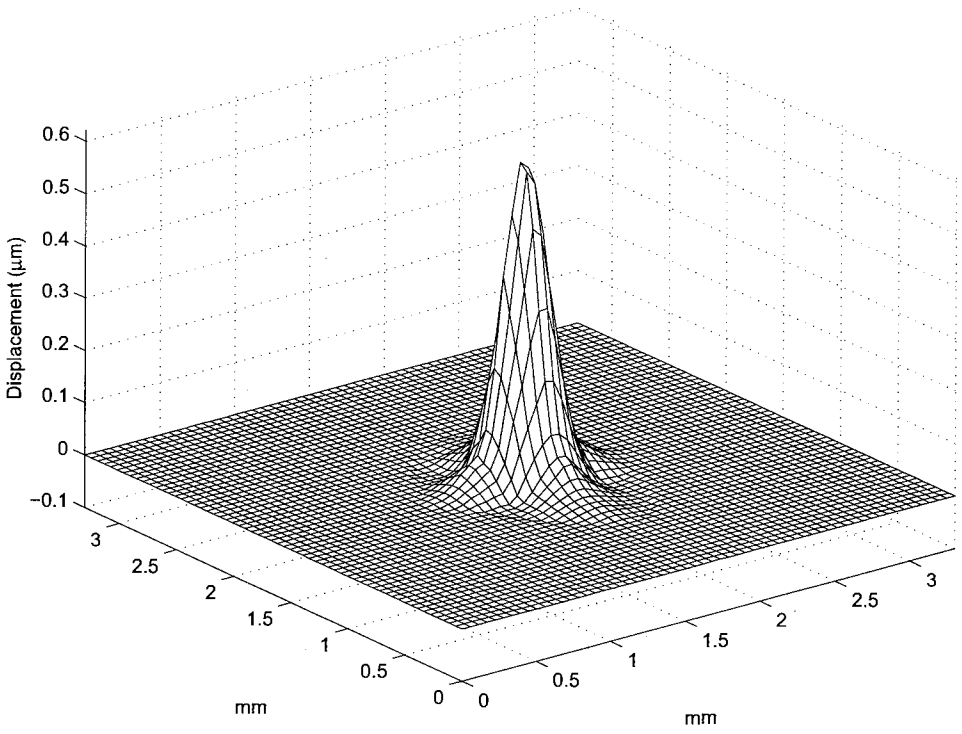

Figure 6.6: Deformable mirror single actuator influence function at 75%.

surface has been centered in a grid with the same extent as the full DM to clearly show the range of influence. 0 degree and 45 degree cross sections are shown in Figure 6.7. Actuator coupling along 0 degrees was 13.5% at the first neighboring actuator, and reduced to 1% at the second. Along 45 degrees, there is negligible coupling to the nearest actuator.

To investigate the potential error in reconstructing a surface shape by superpositioning of single actuator responses, individual and combined responses of two adjacent actuators were measured using an Adaptive Optics Associates mini-Wavescope wavefront sensor. The image of the DM was magnified by 1.6X to fill the wavefront sensor and achieve better sampling with the supplied 133 μm pitch lenslets. The reported optical path difference was scaled down by the 1.6X magnification factor.

Cross-sections through the peaks of the influence functions are shown in Figure 6.8. The superimposed responses underestimate the actual maximum displacement when both actuators were pushed simultaneously by 6.8 %. The maximum absolute error observed was

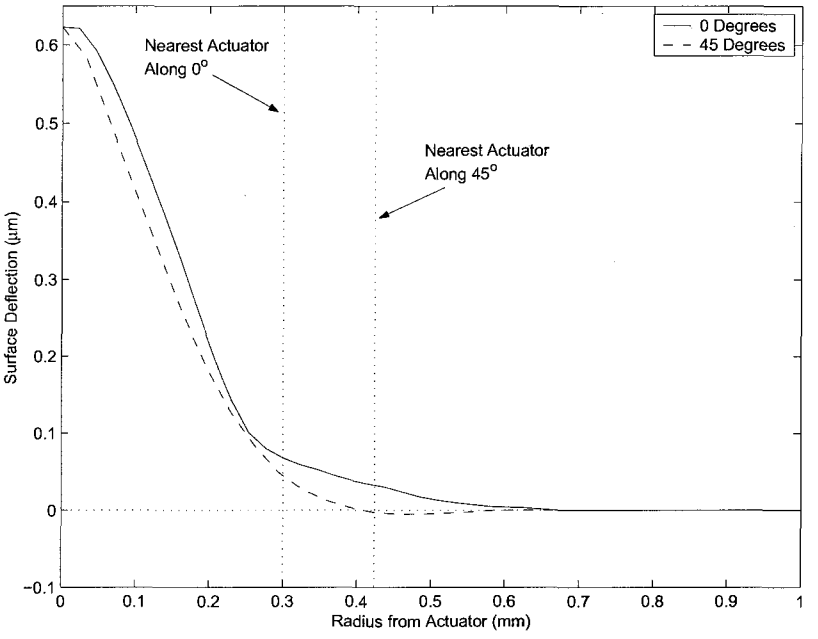

Figure 6.7: 0° and 45° cross-sections of DM influence function.

7.8 %. This error is not accounted for in the zonal control scheme because each actuator is poked individually, whereas the modal control scheme should provide a more accurate measure of surface shapes.

Another important aspect of the DM revealed by this test is that the displacement response is not uniform across all actuators.

6.2.4 Zernike Mode Representation

Zernike modes are commonly used as a modal control basis for AO systems since they describe optical aberrations over a unit circle. It is, therefore, of interest to observe this DM's ability to reconstruct Zernike shapes. Noll's definition of Zernike polynomials, modified for statistical description of turbulence, were used [32]:

$$\left.\begin{aligned} Z_n^m &= \sqrt{n+1}R_n^m(r)\sqrt{2}\cos m\theta \\ Z_n^m &= \sqrt{n+1}R_n^m(r)\sqrt{2}\sin m\theta \end{aligned}\right\} \quad m \neq 0$$
$$Z_n^m = \sqrt{n+1}R_n^0(r) \qquad m = 0 \tag{6.4}$$

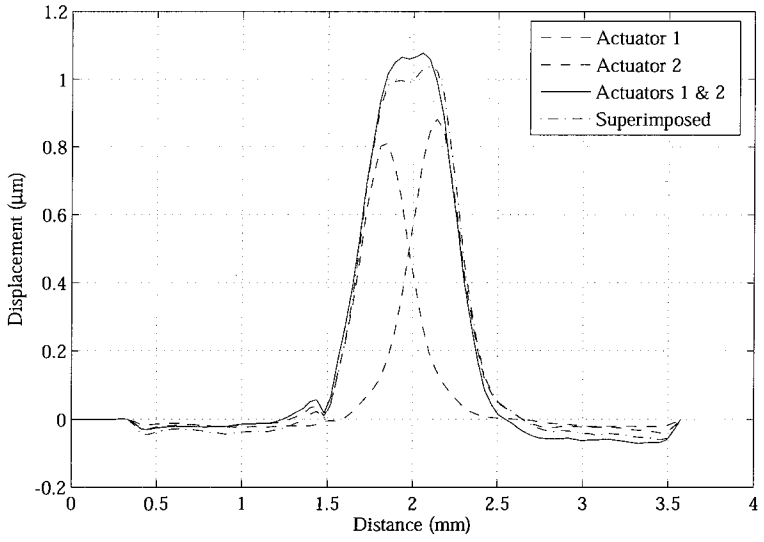

Figure 6.8: Individual, superimposed, and 2-actuator influence function cross-sections.

where

$$R_n^m(r) = \sum_{s=0}^{(n-m)/2} \frac{(-1)^s \quad (n-s)!}{s!\left[(n+m)/2-s\right]!\left[(n-m)/2-s\right]!} r^{n-2s} \tag{6.5}$$

and n and m are always integral and satisfy $m \leq n, n-|m| =$ even. An important property of the Zernike polynomials is that they have an RMS value of one over the unit circle.

A 128 × 128 grid representing the 3.3 × 3.3 mm DM was generated and the Zernike polynomials defined on a circular pupil with diameter of 100 samples, equivalent to 2.5 mm. Using the measured actuator influence function and assuming it to be identical for each actuator, a best fit of the DM to the Zernike surface was calculated. Only the central 80 actuators, as previously shown in Figure 5.2, were used to fit the Zernike surface.

Figure 6.9 shows the RMS displacement of the Zernike mode, the DM fit, and residual error for the first 45 Zernike modes. The data is plotted versus Zernike radial degree (subscript n) while the minor tick marks indicate values of azimuthal frequency (superscript m), in increasing order. The RMS value of the Zernike modes deviates slightly from unity due to the finite sampling grid on which the surfaces were defined. The DM fit is always worst for low azimuthal degree due to the lack of actuators around the pupil circumference to fit the steep edges of these modes. The rapidly increasing residual error suggests that the circular pupil and polar basis functions on the square grid of actuators is inadequate

for representing Zernike shapes of high order.

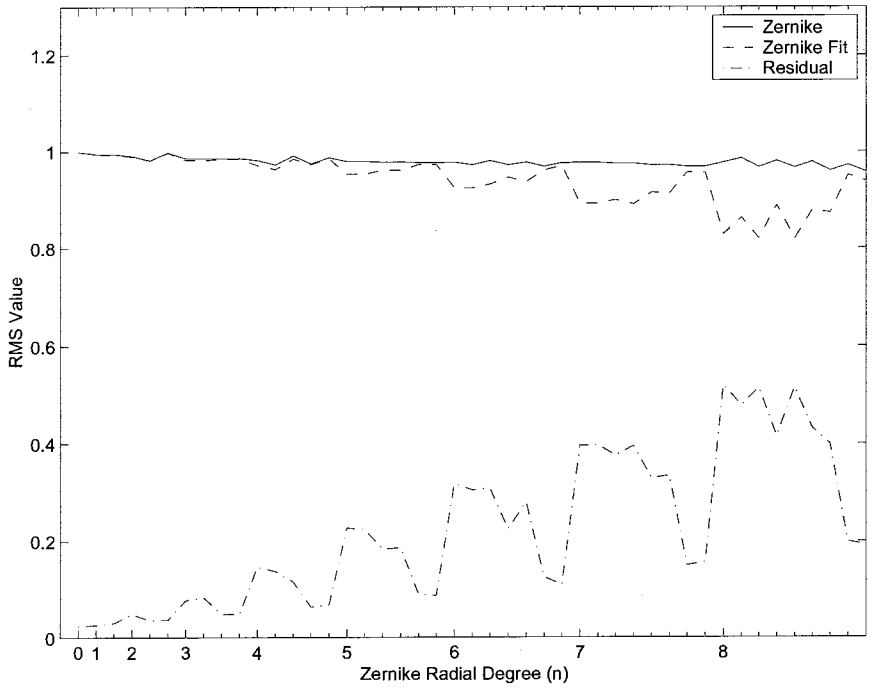

Figure 6.9: RMS displacement of the Zernike mode, DM best fit, and residual error.

Boston Micromachines has also demonstrated a 1024 actuator DM based on the same manufacturing process. To see how this DM technology may scale, a 1024 actuator model was fit to Zernike shapes assuming the same actuator influence function. The results are shown in Figure 6.10. The 1024 actuator DM RMS displacement is indistinguishable from the finite sampled Zernike modes. The residual error has also been reduced dramatically for all modes.

Figures 6.11 and 6.12 show sample Zernike surfaces for astigmatism $\left(Z_2^2\right)$ and a high-order mode $\left(Z_6^6\right)$, the 140 actuator DM fit to the Zernike mode, the DM surface masked by the pupil, and the residual error of the fit within the pupil.

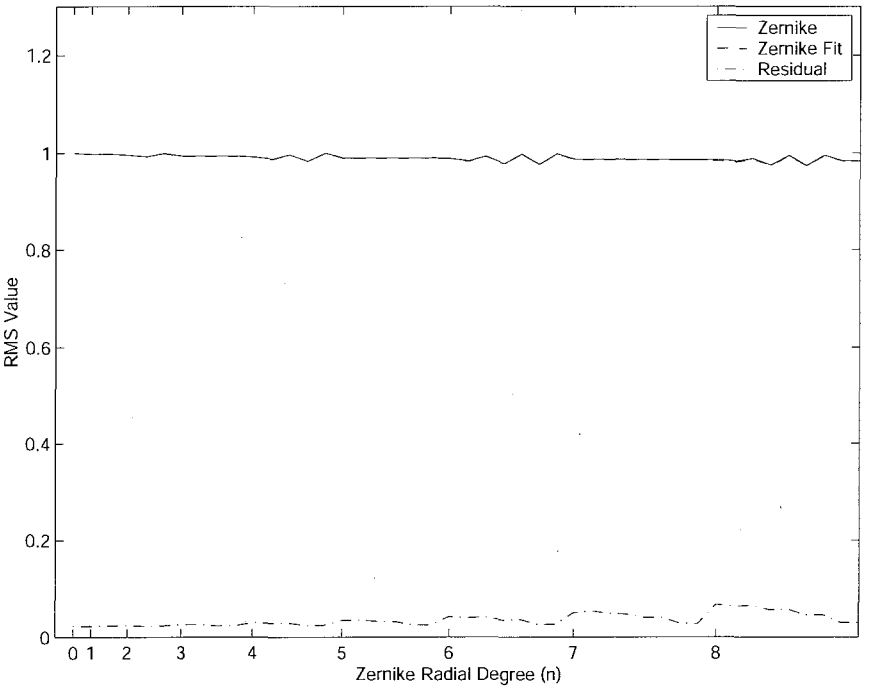

Figure 6.10: RMS displacement of the Zernike mode, DM best fit, and residual error for a 1024 actuator DM.

6.3 Wavefront Sensor Characterization

6.3.1 Noise

There are a number of noise factors common to CCD cameras. These can generally be categorized as fixed-pattern noise sources and illumination response non-uniformity.

Overscan

The overscan region of a CCD is typically a small number of rows or columns of the frame not exposed to light. This region can contain high or low counts that affect image operations and should be removed. Figure 6.13 below shows a line profile from a flat field image. The overscan region can be identified by the sharp drop in counts at the right-most edge. For this camera, the overscan region occupies three rows of the CCD image.

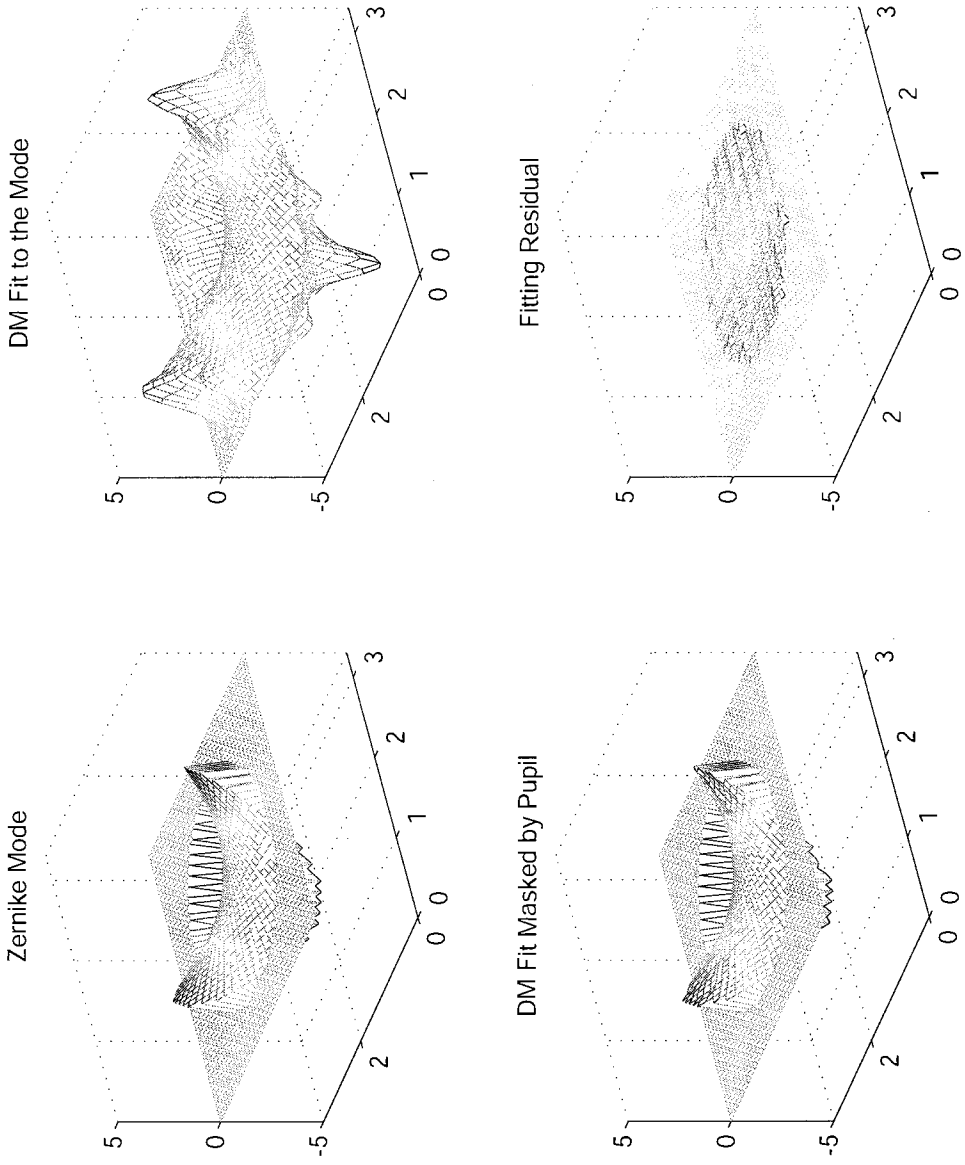

Figure 6.11: DM surface fit to Z_2^2

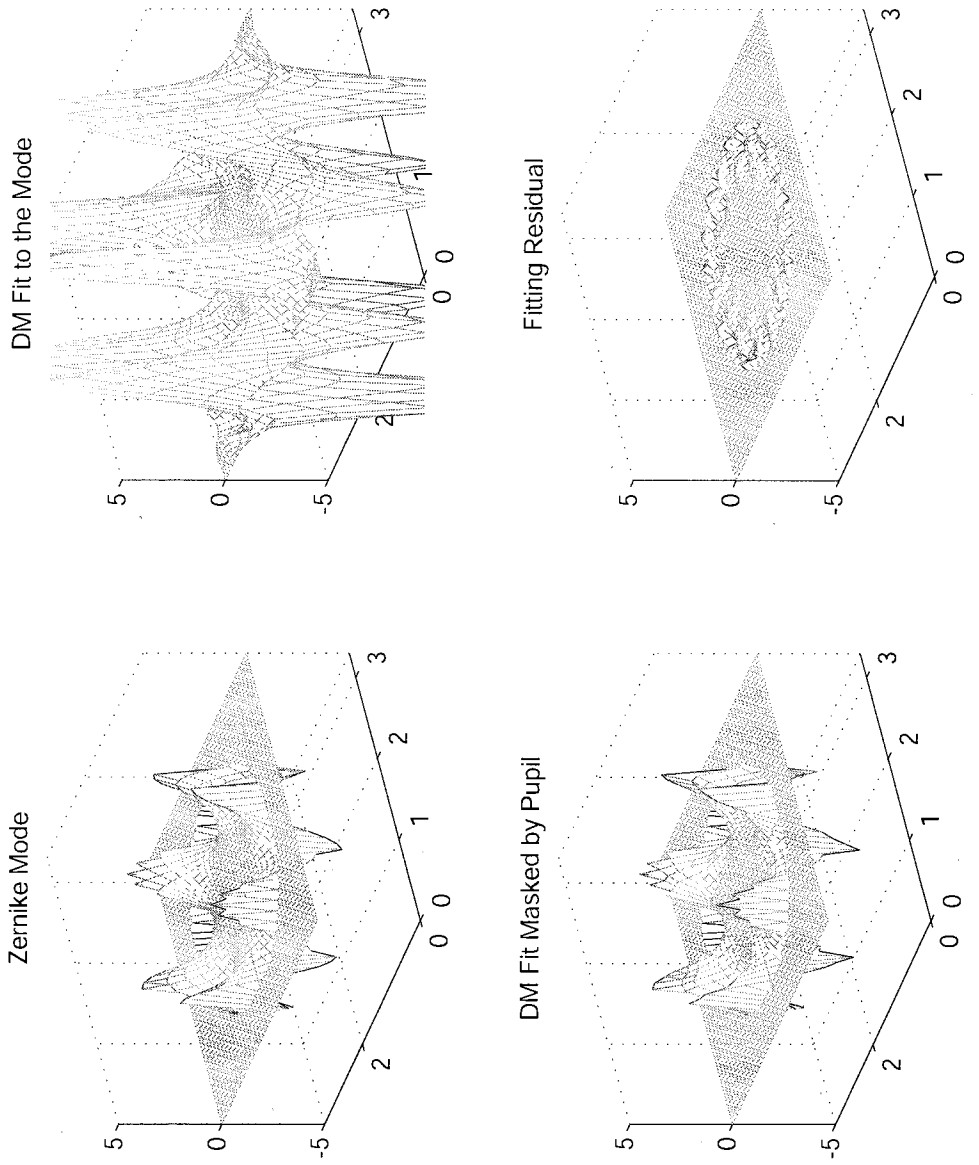

Figure 6.12: DM surface fit to Z_6^6

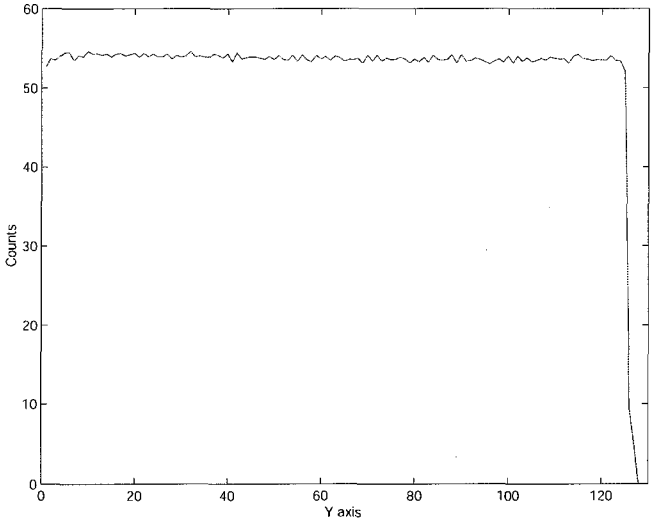

Figure 6.13: Flat field image cross-section with overscan region.

Bias

CCD devices normally have a bias current applied to the sensor to ensure that it operates in a linear regime. A side-effect of applying this current is that the CCD will always read a non-zero count. This level may vary over time and with temperature changes. The effect of the bias current can be seen by capturing a zero second exposure. While we were unable to capture a zero second exposure with the camera configuration, a series of frames were acquired at maximum frame rate with a threaded lens cap on the camera. The average of these frames is shown in Figure 6.14. The mean level in camera counts is 3.01 with a slightly greater response along the leading X edge, and a lower response on the leading Y edge. A mean bias frame should be subtracted from all image data.

Flat Field

Variations in the silicon or manufacturing process cause individual pixels to exhibit different light response curves, or there may be a gradient across the CCD. To compensate for this, a flat field image is generated. The flat field image is an average of a number of evenly illuminated frames. A flat field image taken from the science camera, shown in Figure 6.15, shows a significantly non-uniform response across the pixels.

To apply the correction, image data is divided by the flat field image and then rescaled

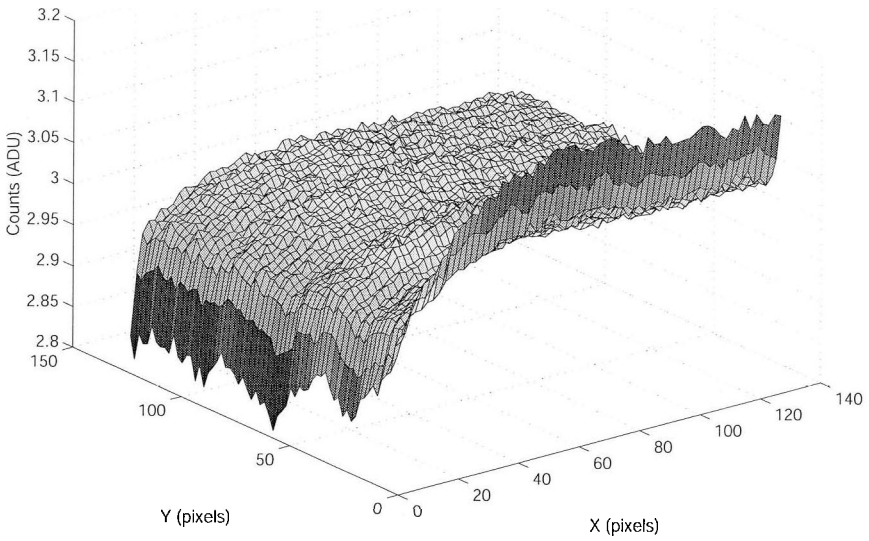

Figure 6.14: Average of 5000 bias frames with overscan removed.

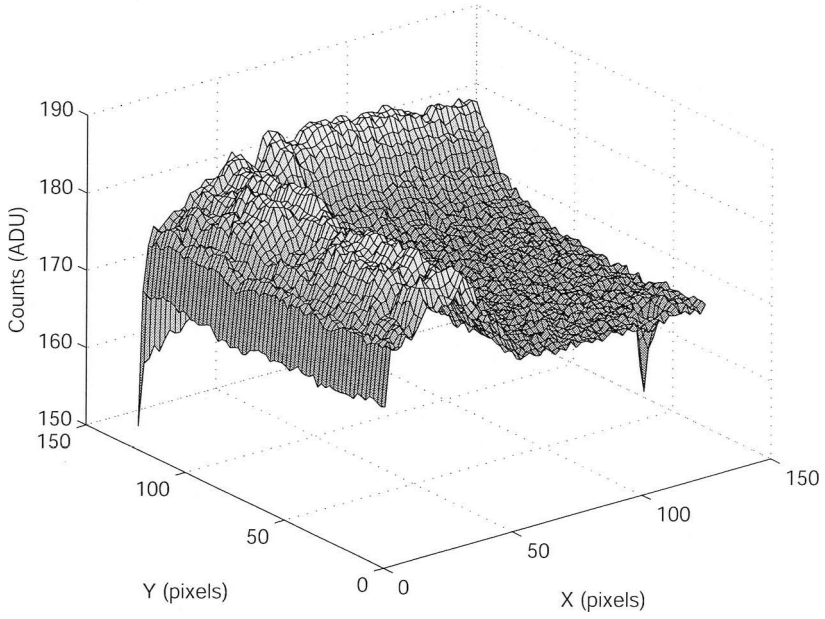

Figure 6.15: Flat field image.

by the mean level of the flat field. This correction normalizes the response of all pixels in the image.

All frames should have their overscan region removed and then follow the image reduction procedure as described in Equation 6.6.

$$\text{final frame} = \frac{(\text{image} - \text{bias})}{(\text{flat} - \text{bias})} (\text{mean}\,(\text{flat})) \tag{6.6}$$

External Noise

It was observed that the spot centroids of the wavefront sensor varied considerably in open loop when there was no source of turbulence. The plot in Figure 6.16 shows the variation in the centroid computation of one axis for a sample spot. The standard deviation of the variation is 0.03 pixels, which is a significant error that is passed through the reconstructor to the DM. The source of this noise is not necessarily the camera itself; it could be due to laser speckle noise or ambient air currents in the room.

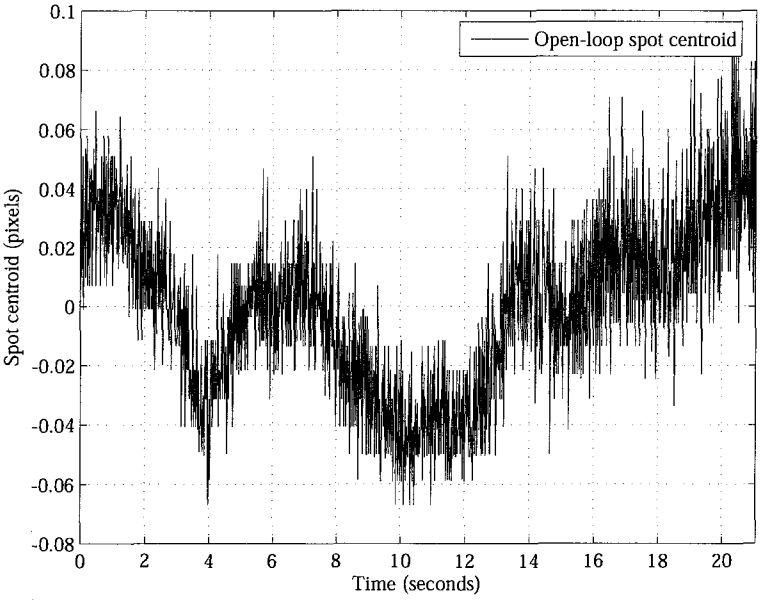

Figure 6.16: Open loop centroid variation without turbulence.

6.3.2 Frame Rate

Though rated for operation at 736 fps, the Dalsa CA-D1-0128A with QRTS drivers under the QNX operating system was only able to achieve a maximum frame rate of 522 fps. During closed loop operation, the write time to the DM was a limiting factor of the closed loop sampling rate. The maximum bandwidth of the IO interface was 100 kHz and due to the nature of the write signals, a full write to the DM was completed at a frequency of approximately 330 Hz. To avoid dropped frames from the camera, it was decided to operate the wavefront sensor with an integer divisor of the maximum frame rate, 261 fps.

6.4 Image Quality

AO system performance can be assessed from two perspectives: science image quality and control system frequency response. Atmospheric turbulence has the effect of blurring an astronomical image. For a given exposure time, the image illuminance will be spread over a larger area, reducing the peak signal strength while redistributing that power into the wings of the profile. For an illustration of this, see Figure 6.17. The AO system's goal is to restore the image to a diffraction limited state with as much illumination power in the central Airy disc. Three commonly used means of measuring the distribution of illuminance are the Strehl improvement ratio, full width at half maximum, and encircled energy.

The Strehl improvement is a commonly used optical system performance metric. It is the ratio of the illuminance at the peak of an aberrated point image to that of an aberration-free image formed by the same optical system. The Strehl improvement can be calculated from CCD images using the following:

$$\text{Strehl} = \frac{\max(I)}{\max(I_0)}, \tag{6.7}$$

where the subscript 0 indicates the aberration-free image.

The Strehl ratio gives a measure of how much of the central intensity is restored by the AO system. A larger Strehl ratio indicates that the core of the image is closer to the maximum reference image intensity. Since the Strehl ratio is an image quality measurement

it is derived from data obtained by the science camera.

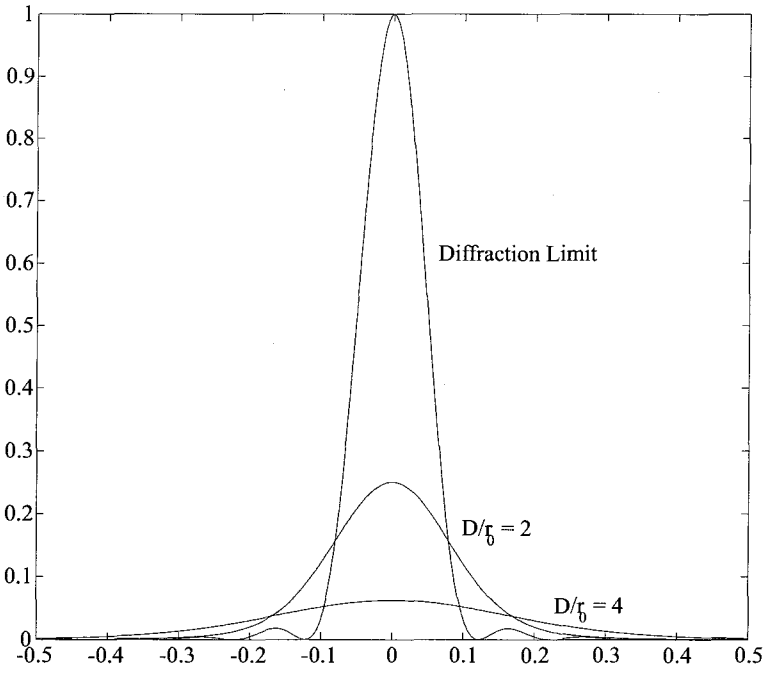

Figure 6.17: Theoretical diffraction limited and turbulence limited point spread functions.

While the Strehl ratio gives a measure of peak intensity, it does not give any indication of the broadness of the intensity profile. One such measure is the full-width at half-maximum (FWHM). As is implied by the term, this performance metric is a measure of the width of the illumination profile at one half of the peak intensity. A smaller FWHM is desirable, generally indicating a better resolution in the science image.

The encircled energy is another measure of the broadness of the illumination distribution. This performance metric is a measure of the radius about the peak that contains a given percentage of the total illumination in the image. This can be of importance for designing accompanying instruments such as spectrographs where light throughput for a given aperture is important but not the distribution.

A second Dalsa digital camera, identical to the WFS camera, was placed at the science focus of Figure 2.4 to record image data. To allow for longer exposures with the limited dynamic range of this camera, an average of multiple frames was performed in software.

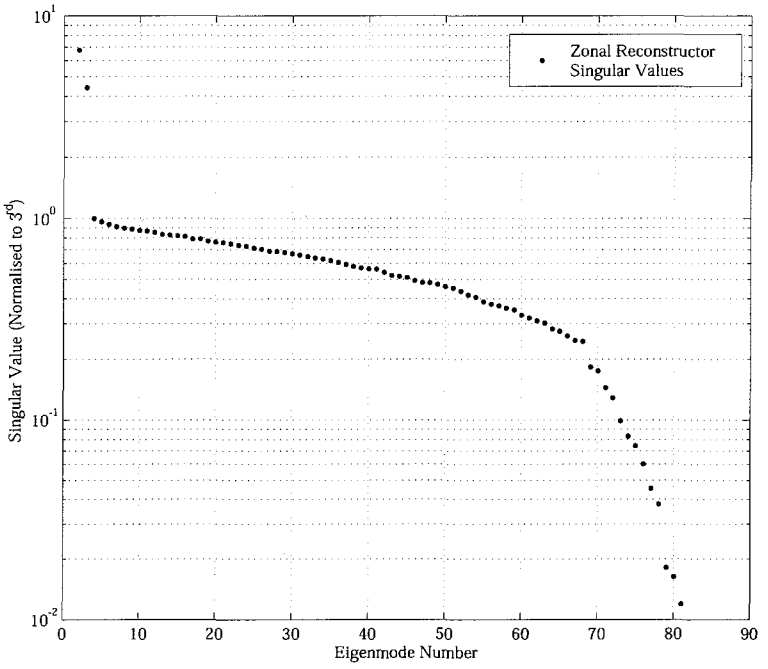

Figure 6.18: Singular values of the zonal reconstructor normalised to the first DM eigenmode.

6.4.1 Zonal Controller

The controller design allowed for tuning of the SVD threshold to optimize system performance. For a fixed level of turbulence, the SVD cutoff threshold was varied and science images acquired for each setting. Exposures of 150,000 frames were accumulated to mitigate the impact of system noise and correlated measurements of turbulence. The thresholds used were relative to the third singular value of the system, which corresponded to the first eigenmode of the system incorporating the DM (the first two singular values correspond to the tip-tilt mirror). In Figure 6.18 the singular values of the zonal reconstructor are shown normalised to the third value.

The Strehl improvement ratio for selected SVD cutoffs for the zonal controller is plotted in Figure 6.19. The dashed line shows a Strehl ratio of 0.21 for the uncorrected turbulence ($\Delta T = 130°C$). The dash-dot line indicates the Strehl for correction with the tip-tilt mirror alone and the DM held in its flat state. By referring to Figure 6.18, one can determine the number of controlled eigenmodes of the system from the SVD cutoff threshold. A high threshold indicates that the AO system is operating with very few eigenmodes. When the

DM was operating, a high cutoff reduced the mirror's ability to compensate for turbulence by limiting the surface shapes it could produce. With a cutoff of 0.8 the DM had been limited to operating with only 13 eigenmodes and the performance was reduced to nearly that of the tip-tilt mirror alone.

As the cutoff was reduced and more eigenmodes controlled, a peak was reached at an SVD threshold of 0.3. Normally this would be the optimum number of operating modes for the DM, further modes should be poorly sensed by the system and detract from the performance. This decreasing trend was observed as the threshold was further reduced from 0.3, however a large gain in Strehl was observed for thresholds of 0.05 and 0.02.

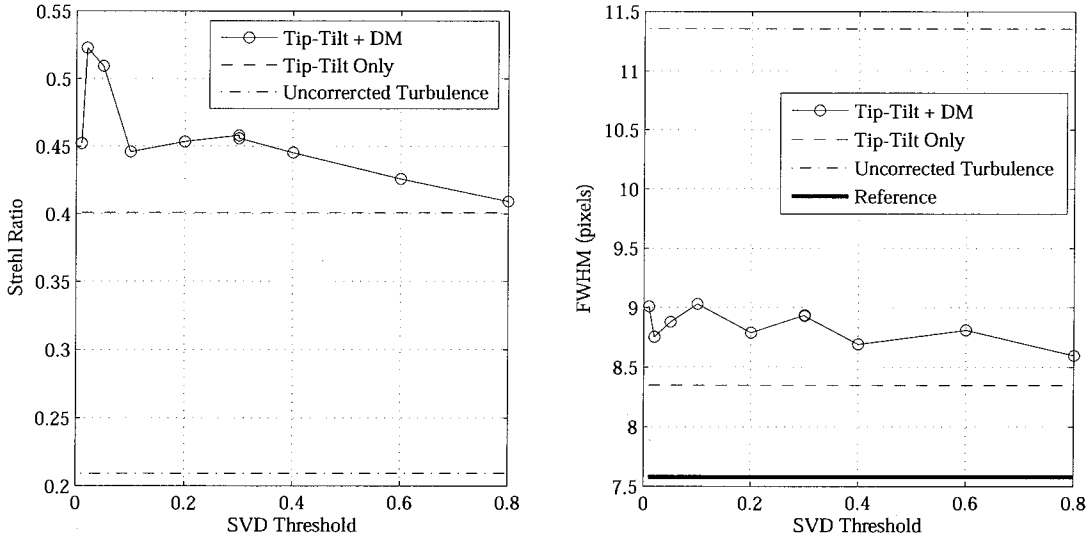

Figure 6.19: Strehl ratio and FWHM for the zonal controller as a function of SVD cutoff.

To explain this behaviour it is necessary to examine the eigenmode matrix, $\mathbf{V}$. Recall from Section 5.1 that a row of the V matrix shows the coefficient of an actuator in each eigenmode of the system. A plot of the first row of $\mathbf{V}$ (corresponding to a tip-tilt actuator usage in each eigenmode) in Figure 6.20 shows that the tip-tilt mirror was not completely isolated from the DM. This is apparent due to the non-zero components beyond the first two eigenmodes, particularly in the eigenmodes beyond 70. This implies that during turbulence, the full correction of tip and tilt requires the use of these eigenmodes with small singular values. Since tip and tilt is the strongest component of turbulence, the increased residual error due to incomplete correction severely impacts the Strehl ratio. When the

SVD threshold was set small enough, the inclusion of these eigenmodes provided a boost to the image quality.

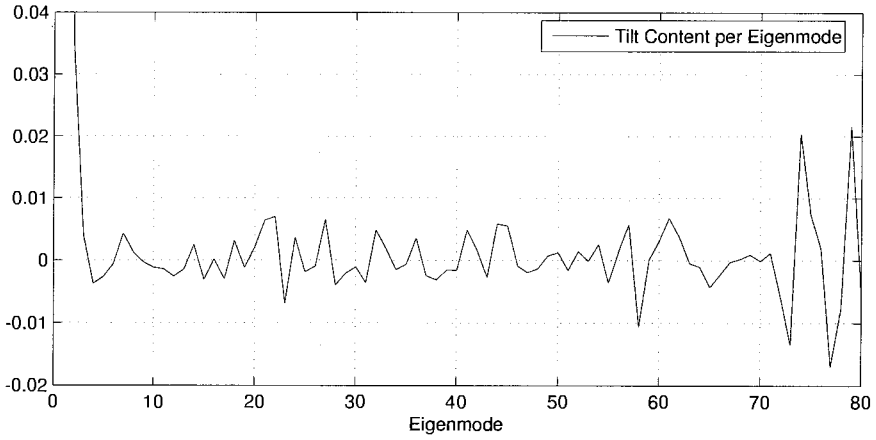

Figure 6.20: Tilt actuator content for each eigenmode of the Zonal SVD.

Using an SVD threshold of 0.02 and varying the gain of the system yielded image quality results as shown in Figure 6.21. A low gain limited the controller's ability to correct for turbulence before the phase state changed. As the gain of the system was increased, the Strehl ratio progressively increased. The stability of the simple integrator in the zonal controller was marginal as a gain of 0.5 was reached and large fluctuations in Strehl ratio were observed. At a gain of 0.56 the zonal controller was amplifying noise to the point where the Strehl ratio was severely degraded.

When considering the full width at half maximum for the same image data it can be seen in Figure 6.19 that the FWHM remained mostly independent of changes to the SVD threshold. However, as the gain was increased in Figure 6.21, the FWHM very nearly reached the same value as that for the reference image. It is interesting to note that the best Strehl ratio and FWHM measures were not achieved at the same gain. It is unclear why tip-tilt control alone provided the best FWHM measure.

6.4.2 Modal Controller

A similar set of image quality tests were performed with the modal controller. A basis set of 44 modes of the form described in Table 5.1 was used in the formation of the modal reconstructor. Immediately apparent from the singular values plotted in Figure 6.22, the

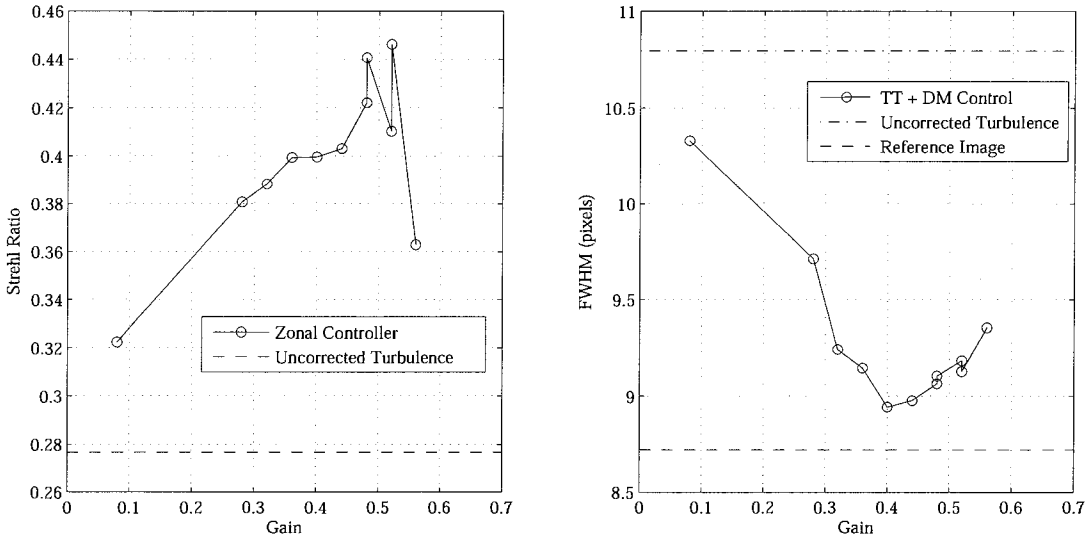

Figure 6.21: Strehl improvement ratio and FWHM as a function of zonal controller gain. (SVD threshold set to 0.02)

tip and tilt modes are no longer dominant in the system because the DM modes are much more easily detected than the zonal single actuators.

The temperature difference in the turbulence generator was reduced slightly to $\Delta T = 100°C$ for stability reasons. This reduced the impact of the turbulence, giving an uncorrected Strehl ratio of 0.31. As the SVD threshold was varied in the controller, the Strehl ratios shown in Figure 6.23 were observed. The impact of cutting a large number of eigenmodes was much more pronounced with the modal controller, reducing performance to nearly that of uncorrected turbulence. As the threshold was lowered, a peak was observed with a cutoff of 0.163. Allowing the next eigenmode dramatically reduced the system performance, while also allowing the following eigenmode restored it. With an SVD cutoff less than 0.135 the Strehl ratio progressively fell to below the level of tip-tilt correction alone.

The maximum Strehl ratio achieved by the modal controller was lower than that with the zonal controller, even with lower turbulence. This may be due to the dead actuators of the DM. Since the dead actuators remain at a zero displacement, while the modes are intended to have a mean displacement about mid-stroke, they may have a detrimental effect on the DMs ability to generate the desired shape.

With the modal reconstructor, one of the tilt actuators was very strongly controlled

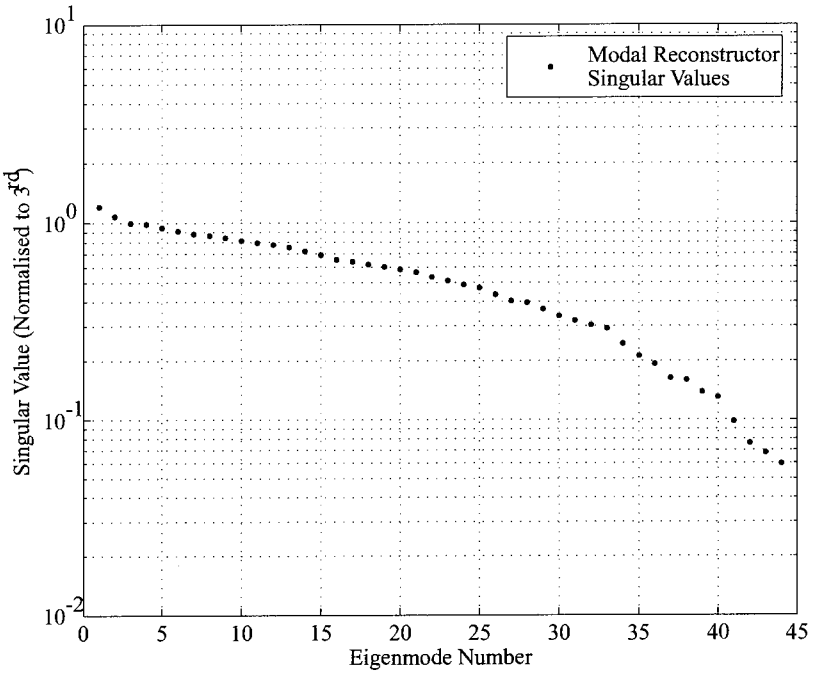

Figure 6.22: Singular values of the modal reconstructor normalised to the third eigenmode.

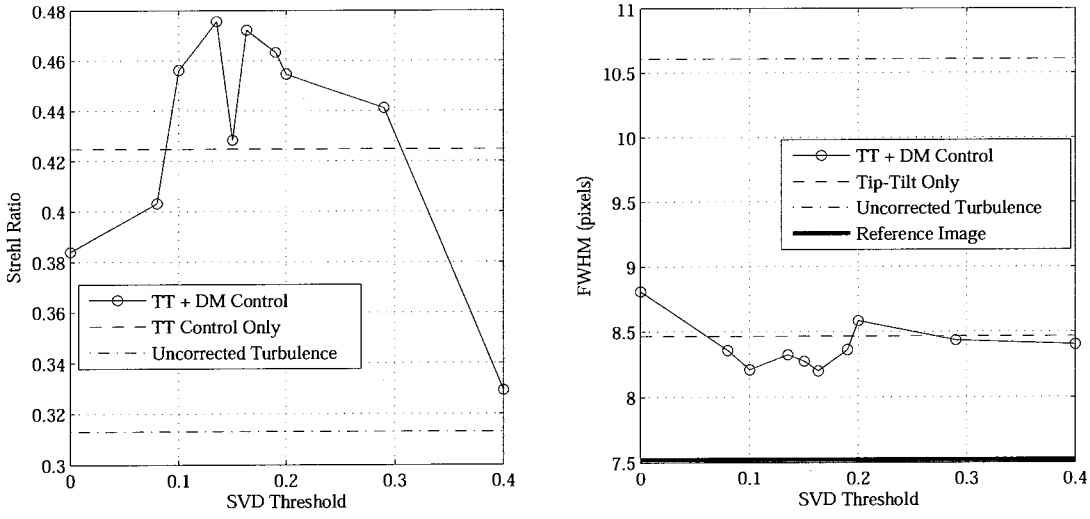

Figure 6.23: Strehl improvement ratio and FWHM for the modal controller as a function of SVD cutoff.

by many eigenmodes of the system. Figure 6.24 shows the magnitude of this actuator's response for each eigenmode of the system. This strong coupling to many eigenmodes was seen for many of the basis modes, suggesting that the mathematically orthogonal basis set of Table 5.1 is not orthogonal in the wavefront sensor space. It is likely that the distribution of basis modes among many eigenmodes accounts for the rapid falloff in the Strehl ratio as higher SVD thresholds were used.

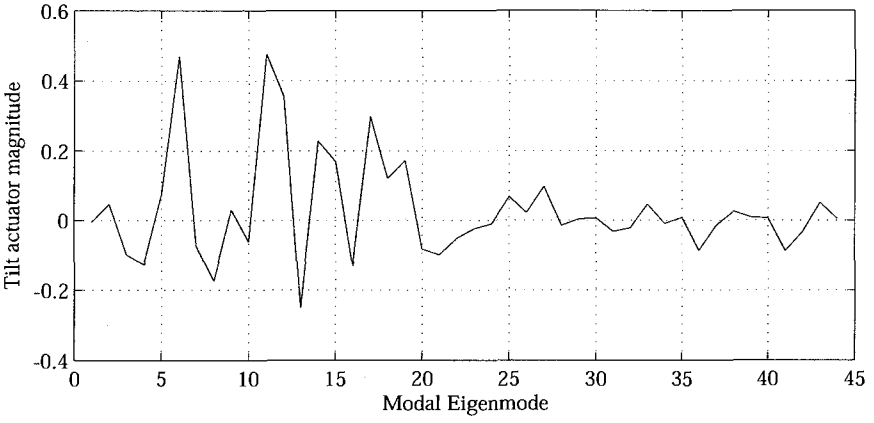

Figure 6.24: Tilt actuator magnitude in modal eigenmodes.

Having selected an SVD threshold of 0.163, the gain of the controller was modified and the Strehl improvement observed. The gains to the DM and the tip-tilt actuators were set equal. The modal controller allowed for a wide range of gain values to be tested. Figure 6.25 shows the Strehl improvement as the gain was increased from 0.3 to 1.9. The best performance was achieved with a gain of 1.7; at 1.9 amplification of noise began to be a problem and the performance fell. A gain of 2.0 was unstable.

Considering the FWHM measurements for both SVD threshold (Figure 6.23) and controller gain (Figure 6.25) measurements, improvement to the FWHM corresponds well with improvement to the Strehl improvement ratio. The FWHM reached its smallest value with an SVD threshold of 0.163. At this point, the FWHM was slightly improved over tip-tilt control alone. Although the Strehl improvement was reduced with a large SVD threshold, the FWHM continued to perform well. When the gain was varied, the FWHM steadily improved up to a gain of 1.7.

To compare the encircled energy for each controller, sample images were selected with

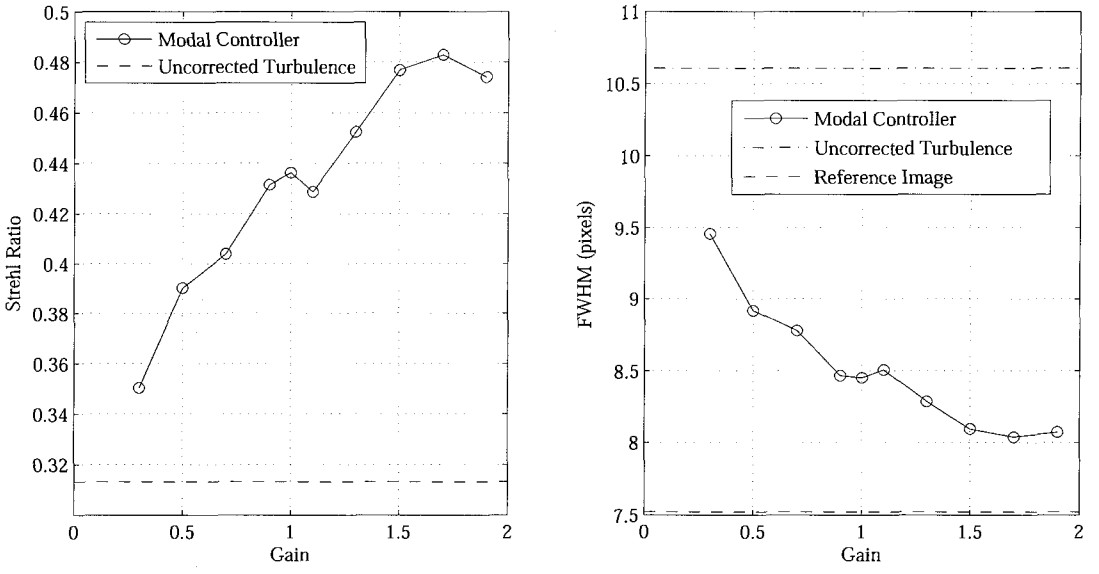

Figure 6.25: Strehl ratio and FWHM as a function of modal controller gain. (SVD threshold set to 0.163)

similar Strehl and FWHM performance. The image from the zonal controller had a Strehl of 0.445 and FWHM of 8.69 pixels (SVD threshold : 0.4, gain : 0.4) while the modal controller image had a Strehl of 0.436 and a FWHM of 8.45 pixels (SVD threshold : 0.163, gain : 1.0). In Figure 6.26 it can be seen that for a small radius, the encircled energy from each controller is very similar. However, the modal controller was more effective at containing more illumination in a smaller radius.

6.5 Frequency Response

Considering control system performance, the rejection transfer function, or rejection ratio, is of primary importance. The rejection transfer function is the ratio of the actuator or modal error to the system input in the frequency domain. The zero dB point in the rejection ratio indicates the frequency at which the system is no longer capable of attenuating the phase error. The frequency of the zero dB point is referred to as the system bandwidth. A ratio greater than zero dB indicates that the controller is amplifying the error at that frequency.

The rejection transfer function of both zonal and modal controllers for one of the tip-tilt actuators is shown in Figure 6.27. The response is typical of the response for any

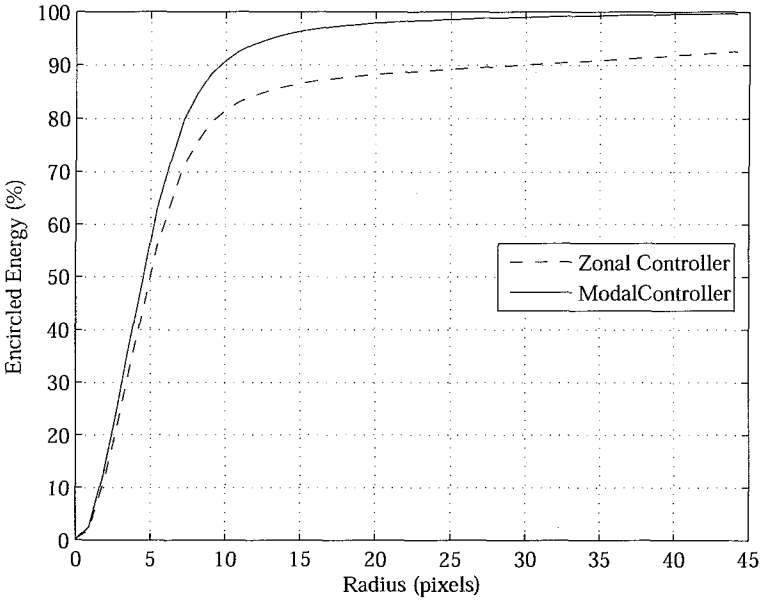

Figure 6.26: Encircled energy for modal and zonal controllers.

actuator/mode of the controllers. The rejection ratios are shown with frequency normalised to the sampling rate of 261 Hz. The performance should scale with increased camera speed to the limit of the mechanical bandwidth of the mirrors thus these give a performance measure of the controllers independent of the sampling rate. Both the zonal and modal controllers have a -20 dB per decade fall-off to low frequency. The variation at low frequency is most likely due to quantization noise.

With a gain of 0.4, the zonal controller had a bandwidth of 6.1% (15.9 Hz) of the sampling rate. At a gain of 1.0, the modal controller had a slightly larger bandwidth of 6.8% (17.7 Hz). When the gain of the modal controller was increased to 1.3, the bandwidth rose to 7.8% (20.3 Hz) at the cost of increased amplification of the error at high frequency. At higher gain, the modal controller also attenuates low frequencies better.

Note that from Figure 2.7, there is significant turbulence power beyond 20 Hz that the controllers are unable to compensate. From this, it can be inferred that the sampling rate is a significant limitation to the AO system's ability to compensate turbulence.

It can be seen that the zonal controller amplified the error at lower frequencies than the modal controller.

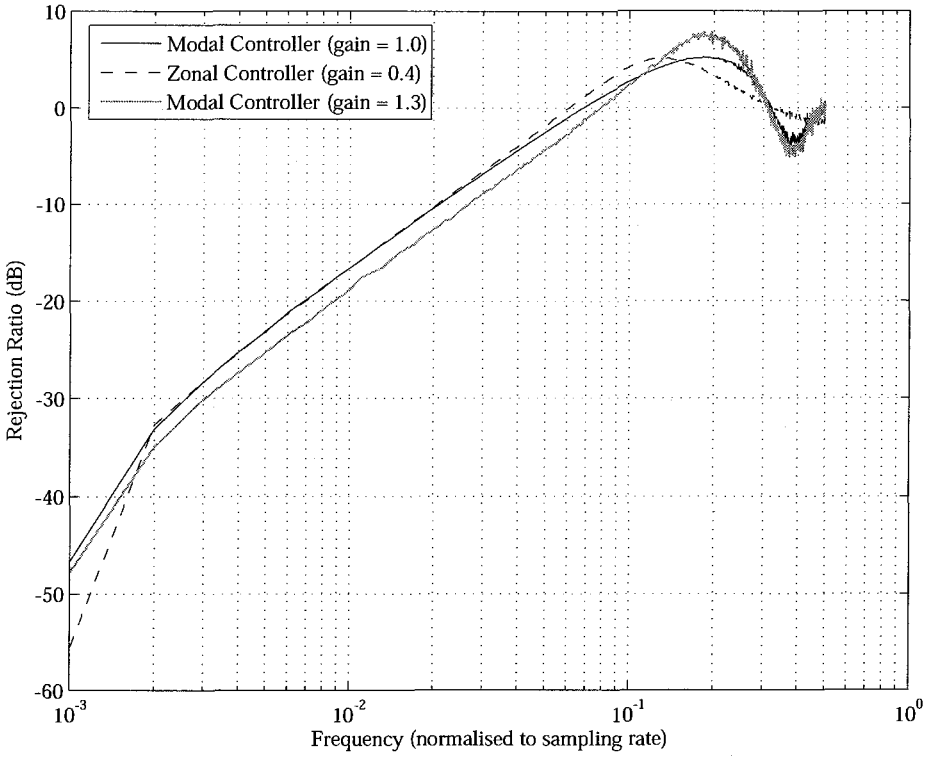

Figure 6.27: Rejection ratios for the zonal and modal controllers (Tilt actuator).

Chapter 7

Conclusion

7.1 Optical Design

A successful optical design for the adaptive optics test-bench was realised using off the shelf components and meeting all of the design requirements. The design incorporated a turbulence generator, tip-tilt mirror, 140 actuator MEMS deformable mirror, Shack-Hartmann wavefront sensor, and a science camera. Though originally envisioned to accommodate varying opto-mechanical components, the magnification factors constrain the optical design to a specific set of hardware. However, by applying the same design principles it would be relatively easy to alter the optical design to include different mirrors or cameras.

7.2 AO System Components

The Dalsa cameras performed adequately in the test-bench environment but were not ideal for use as either the wavefront sensor or science camera. As a wavefront sensor, the camera had a significant amount of noise which is translated into actuator error by the controller. Also, the specified frame rate of 736 fps was never achieved (which may be a limitation of the device drivers or OS), when in fact a frame rate close to 1000 fps is desired to freeze the state of turbulence. The very small CCD size also restricted the ability to sample the wavefront since there was a limitation to how small a lenslet could be manufactured.

As a science camera, the dynamic range of the camera limited the ability to sample

the full point spread function, neutral density filters were required to reduce the peak illumination below saturation at the cost of completely blocking the wings of the profile. A deeper electron well with lower noise and perhaps 12-bit digitizing CCD would be preferable. The resolution and pixel size of the camera were also relatively coarse, a megapixel camera with 8 μm or smaller pixels would be desirable. The high frame rate is also not necessary in a science camera.

The tip-tilt mirror behaved very well, with a perfectly linear response and frequency response greater than that required for the turbulence generated on the test-bench. The slew rate of the mirror might become a problem in extreme turbulence.

The Boston Micromachines deformable mirror proved to be problematic. Dead actuators were a significant problem with this mirror. The already small stroke of approximately 1 μm was restricted to 640 nm in software in an effort to limit the rate of breakage. In cases of large turbulence, the restricted stroke led to clipping of the actuator error.

The quadratic response of the DM can be compensated in software, but gives a varying unit response from low voltage to high voltage. A 12-bit digital-to-analog controller would be desirable to have finer control of the displacement.

The square arrangement of actuators for the DM leads to a high percentage of uncontrolled actuators when working with a circular pupil. The smaller number of actuators within the pupil also limited the spatial frequency of the modes the DM was able to represent. These limitations are mitigated somewhat by the availability of a 1024 actuator DM.

The frequency response of the DM and associated electronics exceeded that required for the test-bench.

7.3 System Performance

Both zonal and modal control of the adaptive optics system were successfully demonstrated. The zonal controller made use of a simple integrator type controller, whereas the modal controller made use of a single integrator with a 2-stage matched delay and filter. Both controllers were capable of partially correcting turbulence, improving image quality in both

peak illumination and width.

One of the primary limitations to both the image quality and bandwidth achieved by the system is the sampling rate. The turbulence simulator generated turbulence with significant power at frequencies greater than the closed loop bandwidth of either controller, 16–20 Hz as tested for the current configuration of the AO system. However, the bandwidths of the controllers scale directly with the sampling rate of the AO system. Without changing the opto-mechanical hardware on the bench, it should be possible to increase the sampling rate of the AO system to the maximum frame rate of the camera by incorporating a different digital IO board for the deformable mirror.

Another potential problem seen with both controllers was the combination of tip and tilt with higher order modes in the reconstructor. It would be desirable to isolate the physically separate mirror responses from each other in the reconstructor.

7.4 Future Work

Continued improvement of the adaptive optics test-bench will be dependent upon increasing the closed loop sampling rate of the system. An upgrade to the digital I/O board controlling the DM should increase the sampling rate to approximately 500 Hz. An upgraded wavefront sensor camera may be required to increase the sampling rate beyond this point.

As a functional closed loop adaptive optics system, several opportunities exist for control system development. A number of aspects to be considered include:

- Investigate an optimal filter and higher order controllers.
- Implement a self-optimizing modal gain controller with individual gains for each eigenmode of the system.
- Isolate physically separate mirrors in the reconstructor.

Results from control system development should be applicable to any adaptive optics system in operation.

Further characterization of the MEMS deformable mirror is also required to improve its performance in an AO system. In particular, the displacement of each actuator needs to be measured to normalise the response across all actuators. A more accurate influence function

model could also be developed by measuring the influence of actuator combinations. Lastly, further investigation of the DM repeatability is necessary.

Bibliography

[1] N. T. Adelman. Spherical mirror with piezoelectrically controlled curvature. *Applied Optics*, 16(12):3075–3077, December 1977.

[2] H. W. Babcock. The Possibility of Compensating Astronomical Seeing. *Publications of the Astronomical Society of the Pacific*, 65:229–236, October 1953.

[3] T. Bifano, J. Perreault, and P. Bierden. A micromachined deformable mirror for optical wavefront compensation. In *High-Resolution Wavefront Control: Methods, Devices, and Applications II*, volume 4124, pages 7–14. SPIE, 2000.

[4] T. Bifano, J. Perreault, P. Bierden, and C. Dimas. Micromachined Deformable Mirror for Adaptive Optics. In *High-Resolution Wavefront Control: Methods, Devices, and Applications IV*, volume 4825, pages 10–13, 2002.

[5] T. G. Bifano, J. Perreault, R. Krishnamoorthy Mali, and M. N. Horenstein. Micro-electromechanical Deformable Mirrors. *IEEE Journal of Selected Topics in Quantum Electronics*, 5:83–89, January 1999.

[6] E. Carrasco, A. Carramiñana, J. L. Avilés, and O. Yam. Optical Seeing at Sierra Negra. *Publications of the Astronomical Society of the Pacific*, pages 879–887, July 2003.

[7] E. S. Claflin and N. Bareket. Configuring an electrostatic membrane mirror by least-square fitting with analytically derived incluence functions. *Journal of the Optical Society of America A*, 3(11):1833–1839, November 1986.

[8] J. C. Dainty, A. V. Koryabin, and A. V. Kudryashov. Low-order adaptive deformable mirror. *Applied Optics*, 37(21):4663–4668, July 1998.

[9] H. M. Dyck and R. R. Howell. Seeing measurements at Mauna Kea from infrared speckle interferometry. *Publications of the Astronomical Society of the Pacific*, pages 786–791, October 1983.

[10] J. Feinleib, S. G. Lipson, and P. F. Cone. Monolithic piezoelectric mirror for wavefront correction. *Applied Physics Letters*, 25:311–313, November 1974.

[11] F. Forbes, F. Roddier, G. Poczulp, C. Pinches, and G. Sweeny. Segmented bimorph deformable mirror. *Journal of Physics E: Scientific Instruments*, 22:402–405, June 1989.

[12] D. L. Fried. Statistics of a Geometric Representation of Wavefront Distortion. *Journal of the Optical Society of America*, 55:1427–1435, November 1965.

[13] D. L. Fried. Optical Resolution Through a Randomly Inhomogeneous Medium for Very Long and Very Short Exposures. *Journal of the Optical Society of America*, 56:1372–1379, October 1966.

[14] D. L. Fried and G. E. Mevers. Evaluation of r_0 for Propagation Down Through the Atmosphere. *Applied Optics*, 13:2620–2622, 1974.

[15] Ronald P. Grosso and Martin Yellin. The membrane mirror as an adaptive optical element. *Journal of the Optical Society of America*, 67(3):399–406, March 1977.

[16] P. J. Hampton, C. Bradley, and P. Agathoklis. Modal control of a deformable mirror for adaptive optics. In *Accepted for Proc. Of PACRIM.* IEEE, 2005.

[17] J. W. Hardy, J. E. Lefebvre, and C. L. Koliopoulos. Real-time atmospheric compensation. *Journal of the Optical Society of America*, 67:360–369, March 1977.

[18] R. Hudgin. Wave-front compensation error due to finite corrector-element size. *Journal of the Optical Society of America*, 67:393–395, March 1977.

[19] R. Hudgin and S. G. Lipson. Analysis of a monolithic piezoelectric mirror. *Journal of Applied Physics*, 46:510–512, February 1975.

[20] Bill Hulburd and David Sandler. Segmented mirrors for atmospheric compensation. *Optical Engineering*, 29(10):1186–90, October 1990.

[21] Stuart M. jefferies, Michael Lloyd-Hart, E. Keith Hege, and James Georges. Sensing wave-front amplitude and phase with phase diversity. *Applied Optics*, 41(11):2095–2102, April 2002.

[22] L. Jolissaint. *Optique adaptative au foyer d'un télescope de la classe 1 mètre.* PhD thesis, Université de Genève, 2000.

[23] L. Jolissaint, O. Keskin, C. Bradley, B. Wallace, and A. Hilton. Multiple Layers Optical Turbulence Generator. Principle and SLODAR Characterization. Preliminary Results. In *Optics in Atmospheric Propagation and Adaptive Systems VII*, volume 5572, pages 256–261. SPIE, September 2004.

[24] M. Kasper, D. Looze, S. Hippler, R. Davies, and A. Glinderman. Increasing the sensitivity of a Shack-Hartmann sensor. In *Canterbury Conference on Wavefront Sensing and its Applications*, 1999.

[25] O. Keskin. Hot air turbulence generator for multi-conjugate adaptive optics. Master's thesis, University of Victoria, 2003.

[26] O. Keskin, L. Jolissaint, C. Bradley, S. Dost, and I. Sharf. Hot-air turbulence generator for multiconjugate adaptive optics. In *Advanced Wavefront Control: Methods, Devices, and Applications*, volume 5162, pages 49–57. SPIE, December 2003.

[27] A. V. Kudryashov and V. I. Shmalhausen. Semipassive bimorph flexible mirrors for atmospheric adaptive optics applications. *Optical Engineering*, 35(11):3064–3073, November 1996.

[28] Maud Langlois, Roger Angel, Michael Lloyd-Hart, François Wildi, Gordon Love, and Alexander Naumov. High Order, Reconstructor-Free Adaptive Optics for 6-8 meter class Telescopes. In *Beyond Conventional Adaptive Optics*, 2001.

[29] R. B. Leighton. The amateur scientist: Concerning the problem of making sharper photographs of the planets. *Scientific American*, pages 157–+, June 1956.

[30] David R. Lide, editor. *CRC Handbook of Chemistry and Physics.* CRC Press, Cleveland, OH, 84 edition, 2003.

[31] R. D. McClure, W. A. Grundmann, W. N. Rambold, J. M. Fletcher, E. H. Richardson, J. R. Stillburn, R. Racine, C. A. Christian, and P. Waddell. An Image Stabilization High-Resolution Camera for the Canada-France-Hawaii Telescope. *Publications of the Astronomical Society of the Pacific*, 101:1156–+, December 1989.

[32] R. J. Noll. Zernike polynomials and atmospheric turbulence. *Journal of the Optical Society of America*, 66(3):207–211, 1976.

[33] C. Paterson, I. Munro, and J. C. Dainty. A low cost adaptive optics system using a membrane mirror. *Optics Express*, 6(9):175–185, April 2000.

[34] Richard G. Paxman, Timothy J. Schulz, and James R. Fienup. Joint estimation of object and aberrations by using phase diversity. *Journal of the Optical Society of America A*, 8(7):1072–85, July 1992.

[35] J. A. Perreault, P. A. Bierden, M. N. Horenstein, and T. G. Bifano. Manufacturing of an optical quality mirror system for adaptive optics. In *High-Resolution Wavefront Control: Methods, Devices, and Applications III*, volume 4493, pages 13–20, 2002.

[36] R. Ragazzoni. Pupil plane wavefront sensing with an oscillating prism. *Journal of Modern Optics*, 43(2):289–93, 1996.

[37] François Roddier. Curvature sensing and compensation: a new concept in adaptive optics. *Applied Optics*, 27(7):1223–1225, April 1988.

[38] Michael C. Roggerman and Bryon Welsh. *Imaging through Turbulence.* CRC Press, Boca Raton, FL, 1996.

[39] G. Rousset, J. C. Fontanella, P. Kern, P. Gigan, F. Rigaut, et al. First diffraction-limited astronomical images with adaptive optics. *Astronomy & Astrophysics*, 230:L29–L32, April 1990.

[40] E. Steinhaus and S. G. Lipson. Bimorph piezoelectric flexible mirror. *Journal of the Optical Society of America*, 69:478–+, March 1979.

[41] V. I. Tatarski. *Wave Propagation in a Turbulent Medium.* McGraw-Hill, New York, 1961.

[42] S. Timoshenko and S. Woinowsky-Krieger. *Theory of Plates and Shells.* McGraw-Hill, 2 edition, 1959.

[43] A. Tokovinin, S. Baumont, and J. Vasquez. Statistics of turbulence profile at Cerro Tololo. *Monthly Notices of the Royal Astronomical Society*, 340:52–58, March 2003.

[44] A. Tokovinin, S. Thomas, and G. Vdovin. Using 50-mm electrostatic membrane deformable mirror in astronomical adaptive optics. In *Advancements in Adaptive Optics*, volume 5490, pages 580–585. SPIE, October 2004.

[45] G. A. Tyler. Bandwidth considerations for tracking through turbulence. *Journal of the Optical Society of America*, 11:358–367, January 1994.

[46] G. Vdovin and P. M. Sarro. Flexible mirror micromachined in silicon. *Applied Optics*, 34(16):2968–2972, June 1995.

[47] G. Vdovin and P. M. Sarro. Technology and applications of micromachined silicon adaptive mirrors. *Optical Engineering*, 36(5):1382–1390, May 1997.

[48] J. C. Wyant. Use of an ac heterodyne lateral shear interferometer with real-time wavefront correction systems. *Applied Optics*, 14(11):2622–26, November 1975.

[49] F. Zamkotsian and K. Dohlen. Prospects for moems-based adaptive optical systems on extremely large telescopes. In *Beyond Conventional Adaptive Optics*, 2001.

[50] L. Zhu, S. Pang-Chen, D.-U. Bartsch, et al. Adaptive control of a micromachined continuous-membrane deformable mirror for aberration compensation. *Applied Optics*, 38(1):168–176, January 1999.

Appendix A

Optical Design

A.1 Turbulence Generator Foreoptics

	RDY	THI	RMD	GLA	CCY	THC	GLC
> OBJ:	INFINITY	81.134755			100	100	
STO:	146.45000	3.000000		SF5_SCHOTT	100	100	
SLB: "E0 85mm"							
2:	38.37000	5.010000		SK11_SCHOTT	100	100	
3:	-55.68000	50.000000			100	100	
4:	INFINITY	6.500000		'boroflt'	100	100	
SLB: "Window 1"							
5:	INFINITY	179.500000			100	100	
6:	INFINITY	179.500000			100	100	
SLB: "Turbulence"							
7:	INFINITY	6.500000		'boroflt'	100	100	
SLB: "Window 2"							
8:	INFINITY	50.000000			100	100	
9:	124.12000	8.500000		BK7_SCHOTT	100	100	
SLB: "E0 200mm"							
10:	-87.26000	4.000000		SF5_SCHOTT	100	100	
11:	-253.10000	194.140000			100	100	
12:	INFINITY	51.395642			100	0	
SLB: "Focus"							
13:	1029.79000	2.400000		SF10_SCHOTT	100	100	
SLB: "E0 60mm R"							
14:	29.95000	9.000000		SSKN8_SCHOTT	100	100	
15:	-31.94000	50.000000			100	100	
16:	INFINITY	0.000000			100	100	
SLB: "Iris/pupil"							
IMG:	INFINITY	0.000000			100	100	

SPECIFICATION DATA

EPD	22.00000
DIM	MM
WL	632.80
REF	1
WTW	1
INI	BW
XAN	0.00000
YAN	0.00000
WTF	1.00000
VUX	0.00000
VLX	0.00000
VUY	0.00000
VLY	0.00000

APERTURE DATA/EDGE DEFINITIONS

CA	
CIR S1	12.500000
CIR S2	12.500000
CIR S3	12.500000
CIR S4	50.000000
CIR S5	50.000000
CIR S7	50.000000
CIR S8	50.000000
CIR S9	12.500000
CIR S10	12.500000
CIR S11	12.500000
CIR S13	12.500000
CIR S14	12.500000
CIR S15	12.500000

PRIVATE CATALOG

PWL 656.30 643.80 589.30 546.10 479.90 435.80

'boroflt'1.469160 1.469530 1.471330 1.473110 1.476760 1.480150

REFRACTIVE INDICES

GLASS CODE	632.80
SF5_SCHOTT	1.668457
SK11_SCHOTT	1.561883
'boroflt'	1.469868
BK7_SCHOTT	1.515089
SF10_SCHOTT	1.723087
SSKN8_SCHOTT	1.615139

No solves defined in system

```
No pickups defined in system


INFINITE CONJUGATES
   EFL        -25.4006
   BFL         -5.7268
   FFL        -81.3332
   FNO         -1.1546
AT USED CONJUGATES
   RED        128.0044
   FNO        476.3919
   OBJ DIS     81.1348
   TT         880.5804
   IMG DIS      0.0000
   OAL        799.4456
   PARAXIAL IMAGE
    HT          0.0000
    THI     -3257.1200
   ANG          0.0000
   ENTRANCE PUPIL
    DIA        22.0000
    THI         0.0000
   EXIT PUPIL
    DIA         6.8707
    THI       -13.6595
```

A.2 Wavefront Sensor Path

```
    AO Testbench: WFS Path
              RDY             THI      RMD       GLA          CCY   THC   GLC
OBJ:         INFINITY        INFINITY                        100   100
STO:         INFINITY      100.571230                        100   100
    SLB: "Iris/pupil"
  2:          91.37000        5.700000       BK7_SCHOTT      100   100
    SLB: "EO 150mm"
  3:         -66.21000        2.200000       SF5_SCHOTT      100   100
  4:        -197.71000      146.100000                        100   100
  5:         INFINITY       146.100000                        100   100
  6:         197.71000        2.200000       SF5_SCHOTT      100   100
    SLB: "EO 150mm R"
  7:          66.21000        5.700000       BK7_SCHOTT      100   100
  8:         -91.37000      192.728179                        100   100
  9:         INFINITY      -102.497853  REFL                  100   100
    SLB: "Tip-Tilt"
    XDE:     0.000000   YDE:     0.000000   ZDE:     0.000000   BEN
```

```
      XDC:      100        YDC:      100        ZDC:      100
      ADE:    0.000000     BDE:    45.000000    CDE:    0.000000
      ADC:      100        BDC:      100        CDC:      100

   10:        -61.47000        -6.000000        BK7_SCHOTT          100   100
      SLB: "EO 100mm"
   11:         44.64000        -2.500000        SF5_SCHOTT          100   100
   12:        129.94000       -95.920000                            100   100
   13:         INFINITY       -95.920000                            100   100
      SLB: "Focus 1"
   14:       -129.94000        -2.500000        SF5_SCHOTT          100   100
      SLB: "EO 100mm R"
   15:        -44.64000        -6.000000        BK7_SCHOTT          100   100
   16:         61.47000       -34.620000                            100   100
   17:         INFINITY        -6.250000        BK7_SCHOTT          100   100
      SLB: "Beam Splitter 1"
   18:         INFINITY         6.250000  REFL BK7_SCHOTT          100   100
      XDE:    0.000000     YDE:    0.000000    ZDE:    0.000000   BEN
      XDC:      100        YDC:      100        ZDC:      100
      ADE:    0.000000     BDE:  -45.000000    CDE:    0.000000
      ADC:      100        BDC:      100        CDC:      100

   19:         INFINITY        51.162900                            100   100
>  20:         INFINITY       -51.162900  REFL                      100   PIK
      SLB: "Ref Mirror"
   21:         INFINITY       -12.500000        BK7_SCHOTT          100   100
   22:         INFINITY      -103.331432                            100   100
   23:       -124.12000        -8.500000        BK7_SCHOTT          100   100
      SLB: "EO 200m 2"
   24:         87.26000        -4.000000        SF5_SCHOTT          100   100
   25:        253.10000       -67.810000                            100   100
   26:         INFINITY       -25.400000        BK7_SCHOTT          100   100
      SLB: "Beam Splitter 2"
   27:         INFINITY      -110.667000                            100   100
   28:         INFINITY      -120.909682                            100   100
   29:       -162.43000        -2.400000        SF5_SCHOTT          100   100
      SLB: "EO 125mm"
   30:        -54.55000        -6.000000        BK7_SCHOTT          100   100
   31:         76.28000      -139.105266                            100   100
   32:         INFINITY         0.000000                            100   100
  IMG:         INFINITY         0.064121                            100   100

SPECIFICATION DATA
   EPD         3.90000
   DIM              MM
```

WL	632.80		
REF	1		
WTW	1		
INI	BW		
XAN	0.00000	0.00000	0.00000
YAN	0.00000	0.00429	0.08571
WTF	1.00000	1.00000	1.00000
VUX	0.00000	0.00000	0.00000
VLX	0.00000	0.00000	0.00000
VUY	0.00000	0.00000	0.00000
VLY	0.00000	0.00000	0.00000

APERTURE DATA/EDGE DEFINITIONS

CA		
CIR S2		12.500000
CIR S3		12.500000
CIR S4		12.500000
CIR S6		12.500000
CIR S7		12.500000
CIR S8		12.500000
CIR S9		12.500000
CIR S10		12.500000
CIR S11		12.500000
CIR S12		12.500000
REX S17		6.250000
REY S17		6.250000
REX S19		6.250000
REY S19		6.250000
CIR S20		6.250000
REX S21		6.250000
REY S21		6.250000
REX S22		6.250000
REY S22		6.250000
CIR S23		12.500000
CIR S24		12.500000
CIR S25		12.500000
REX S26		12.700000
REY S26		12.700000
REX S27		12.700000
REY S27		12.700000
CIR S29		12.500000
CIR S30		12.500000
CIR S31		12.500000
CIR S14	EDG	12.500000
CIR S15	EDG	12.500000

```
   CIR S16  EDG            12.500000

PRIVATE CATALOG
   PWL 656.30 643.80 589.30 546.10 479.90 435.80
   'boroflt'1.469160 1.469530 1.471330 1.473110 1.476760 1.480150

REFRACTIVE INDICES
    GLASS CODE                 632.80
   BK7_SCHOTT                1.515089
   SF5_SCHOTT                1.668457

No solves defined in system

PICKUPS
   PIK THI S20 Z1 THI S19 Z1 -1.000000


       This is a decentered system.  If elements with power are
       decentered or tilted, the first order properties are probably
       inadequate in describing the system characteristics.

INFINITE CONJUGATES
   EFL    -0.4280E+06
   BFL     0.2673E+06
   FFL     0.6853E+06
   FNO     0.1097E+06
   IMG DIS     0.0641
   OAL      -345.2818
   PARAXIAL IMAGE
    HT       640.2934
   ANG         0.0857
   ENTRANCE PUPIL
    DIA        3.9000
    THI        0.0000
   EXIT PUPIL
    DIA        2.4358
    THI       -0.1610
```

A.3 Science Path

	RDY	THI	RMD	GLA	CCY	THC	GLC
> OBJ:	INFINITY	INFINITY			100	100	
STO:	INFINITY	100.571230			100	100	
SLB: "Iris/pupil"							
2:	91.37000	5.700000		BK7_SCHOTT	100	100	

```
   SLB: "EO 150mm"
 3:       -66.21000        2.200000       SF5_SCHOTT          100   100
 4:      -197.71000      146.100000                           100   100
 5:        INFINITY      146.100000                           100   100
 6:       197.71000        2.200000       SF5_SCHOTT          100   100
   SLB: "EO 150mm R"
 7:        66.21000        5.700000       BK7_SCHOTT          100   100
 8:       -91.37000      192.728179                           100   100
 9:        INFINITY     -102.497853  REFL                     100   100
   SLB: "Tip-Tilt"
   XDE:     0.000000   YDE:     0.000000   ZDE:     0.000000   BEN
   XDC:      100       YDC:      100       ZDC:      100
   ADE:     0.000000   BDE:    45.000000   CDE:     0.000000
   ADC:      100       BDC:      100       CDC:      100

10:       -61.47000       -6.000000       BK7_SCHOTT          100   100
   SLB: "EO 100mm"
11:        44.64000       -2.500000       SF5_SCHOTT          100   100
12:       129.94000      -95.920000                           100   100
13:        INFINITY      -95.920000                           100   100
   SLB: "Focus 1"
14:      -129.94000       -2.500000       SF5_SCHOTT          100   100
   SLB: "EO 100mm R"
15:       -44.64000       -6.000000       BK7_SCHOTT          100   100
16:        61.47000      -34.620000                           100   100
17:        INFINITY      -12.500000       BK7_SCHOTT          100   100
18:        INFINITY      -51.162900                           100   100
19:        INFINITY       51.162900  REFL                     100   PIK
   SLB: "DM"
   XDE:     0.000000   YDE:     0.000000   ZDE:     0.000000   BEN
   XDC:      100       YDC:      100       ZDC:      100
   ADE:     0.000000   BDE:     0.000000   CDE:     0.000000
   ADC:      100       BDC:      100       CDC:      100

20:        INFINITY        6.250000       BK7_SCHOTT          100   100
21:        INFINITY       -6.250000  REFL BK7_SCHOTT          100   100
   SLB: "Beam Splitter"
   XDE:     0.000000   YDE:     0.000000   ZDE:     0.000000   BEN
   XDC:      100       YDC:      100       ZDC:      100
   ADE:     0.000000   BDE:   -45.000000   CDE:     0.000000
   ADC:      100       BDC:      100       CDC:      100

22:        INFINITY     -103.331432                           100   100
23:      -124.12000       -8.500000       BK7_SCHOTT          100   100
   SLB: "EO 200m 2"
```

```
   24:        87.26000       -4.000000       SF5_SCHOTT          100   100
   25:       253.10000      -67.810000                           100   100
   26:        INFINITY      -12.700000       BK7_SCHOTT          100   100
      SLB: "Beam Splitter 2"
   27:        INFINITY       12.700000  REFL BK7_SCHOTT          100   100
      XDE:    0.000000   YDE:    0.000000   ZDE:    0.000000   BEN
      XDC:     100       YDC:     100       ZDC:     100
      ADE:    0.000000   BDE:  -45.000000   CDE:    0.000000
      ADC:     100       BDC:     100       CDC:     100

   28:        INFINITY      110.667000                           100   100
   29:        INFINITY        1.633000                           100     0
      SLB: "First Image"
   30:        INFINITY      -54.451040  REFL                     100     0
      SLB: "Fold"
      XDE:    0.000000   YDE:    0.000000   ZDE:    0.000000   BEN
      XDC:     100       YDC:     100       ZDC:     100
      ADE:    0.000000   BDE:   45.000000   CDE:    0.000000
      ADC:     100       BDC:     100       CDC:     100

   31:      -214.63000       -2.500000       SF10_SCHOTT         100   100
      SLB: "EO 50mm"
   32:       -21.98000       -9.000000       BAF10_HOYA          100   100
   33:        34.53000     -250.621429                           100   PIM
  IMG:        INFINITY        0.064121                           100   100

SPECIFICATION DATA
   EPD        2.74000
   DIM             MM
   WL         632.80
   REF             1
   WTW             1
   INI            BW
   XAN        0.00000        0.00000        0.00000        0.00000
   YAN        0.00000        0.00404        0.00807        0.06858
   WTF        1.00000        1.00000        1.00000        1.00000
   VUX        0.00000        0.00000        0.00000        0.00000
   VLX        0.00000        0.00000        0.00000        0.00000
   VUY        0.00000        0.00000        0.00000        0.00000
   VLY        0.00000        0.00000        0.00000        0.00000

APERTURE DATA/EDGE DEFINITIONS
   CA
   CIR S2                   12.500000
   CIR S3                   12.500000
```

```
   CIR S4                  12.500000
   CIR S6                  12.500000
   CIR S7                  12.500000
   CIR S8                  12.500000
   CIR S9                  12.500000
   CIR S10                 12.500000
   CIR S11                 12.500000
   CIR S12                 12.500000
   REX S17                  6.250000
   REY S17                  6.250000
   REX S18                  6.250000
   REY S18                  6.250000
   REX S19                  1.650000
   REY S19                  1.650000
   REX S20                  6.250000
   REY S20                  6.250000
   REX S22                  6.250000
   REY S22                  6.250000
   CIR S23                 12.500000
   CIR S24                 12.500000
   CIR S25                 12.500000
   REX S26                 12.700000
   REY S26                 12.700000
   REX S28                 12.700000
   REY S28                 12.700000
   CIR S31                 11.000000
   CIR S32                 11.000000
   CIR S33                 11.000000
   CIR S14  EDG            12.500000
   CIR S15  EDG            12.500000
   CIR S16  EDG            12.500000

PRIVATE CATALOG
   PWL 656.30 643.80 589.30 546.10 479.90 435.80
   'boroflt'1.469160 1.469530 1.471330 1.473110 1.476760 1.480150

REFRACTIVE INDICES
    GLASS CODE                632.80
   SF5_SCHOTT                1.668457
   BK7_SCHOTT                1.515089
   SF10_SCHOTT               1.723087
   BAF10_HOYA                1.667087

SOLVES
   PIM
```

PICKUPS

PIK THI S19 Z1 THI S18 Z1 -1.000000

This is a decentered system. If elements with power are decentered or tilted, the first order properties are probably inadequate in describing the system characteristics.

INFINITE CONJUGATES

EFL	803.7599
BFL	-250.6214
FFL	-3253.8250
FNO	-293.3430
IMG DIS	-250.5573
OAL	105.5491

PARAXIAL IMAGE

HT	0.9620
ANG	0.0686

ENTRANCE PUPIL

DIA	2.7400
THI	0.0000

EXIT PUPIL

DIA	0.6768
THI	-52.0766